

This dissertation has been
microfilmed exactly as received

68-9039

JOBE, John Dewey, 1936-
EXCITATION PROCESSES IN HELIUM.

The University of Oklahoma, Ph.D., 1968
Physics, spectroscopy

University Microfilms, Inc., Ann Arbor, Michigan

THE UNIVERSITY OF OKLAHOMA
GRADUATE COLLEGE

EXCITATION PROCESSES IN HELIUM

A DISSERTATION
SUBMITTED TO THE GRADUATE FACULTY
in partial fulfillment of the requirements for the
degree of
DOCTOR OF PHILOSOPHY

BY
JOHN DEWEY JOBE
Norman, Oklahoma
1968

EXCITATION PROCESSES IN HELIUM

APPROVED BY

Robert M. St. John

C. C. Lin

John L. Loh

S. E. Babby, Jr.

William N. Huff

DISSERTATION COMMITTEE

ACKNOWLEDGMENTS

The author wishes to express his sincere appreciation to Dr. Robert M. St. John, for his suggestions and guidance during this work, for the excellent research facilities, and for the procurement of experimental apparatus of the highest quality.

Special appreciation is extended to Professor Chun C. Lin for many helpful discussions and in particular for his excellent presentation of the theory of atomic physics in formal course work.

The author is grateful for the assistance of Dr. S.J.B. Corrigan on experimental problems. He is also indebted to the assistance of his colleagues Paul N. Stanton and James D. Walker, Jr.

Financial support for the 1965 through 1967 academic years was generously provided by the National Aeronautics and Space Administration under the Graduate Traineeship program.

A large measure of profound gratitude is due my wife, Susan, for her personal sacrifice, patience, and constant inspiration during the course of this work.

TABLE OF CONTENTS

	Page
LIST OF TABLES	vi
LIST OF ILLUSTRATIONS	vii
 Chapter	
I. INTRODUCTION	1
II. DESCRIPTION OF EXPERIMENTAL APPARATUS	5
The Vacuum System	
The Optical System	
The Electronic System	
The One Centimeter Beam Electron Gun	
III. MEASUREMENT OF EXPERIMENTAL PARAMETERS	13
Standardization	
General Experimental Procedure	
IV. ABSOLUTE MEASUREMENTS OF THE 2^1P AND 2^3P ELECTRON EXCITATION CROSS SECTIONS OF HELIUM ATOMS	20
Description of the Experiment	
The Cascading States	
Analysis of Data	
Discussion of Results	
Applications	
V. EXCITATION TRANSFER PROCESSES IN HELIUM	46
Description of the Experiment	
Presentation of Data	
Calculation of Transfer Cross Sections	
Discussion of Results	

TABLE OF CONTENTS (Cont'd.)

	Page
VI. THE TEMPERATURE DEPENDENCE OF EXCITATION TRANSFER	76
Description of Experiment	
Data Acquisition	
Analysis of Data	
Discussion of Results	
VII. CONCLUSION.	99
REFERENCES	103

LIST OF TABLES

Table	Page
I. Values of apparent cross sections for states cascading to the 2^1P and 2^3P states	25
II. Comparison of oscillator strengths for 2^1P state.	42
III. Values of apparent cross sections at high pressure for the 1P and D states	49
IV. Values of apparent cross sections at high pressure for the F states.	57
V. Transition probabilities for F to D transitions	59
VI. Contributions to apparent cross section of the D states	66
VII. Values for $^1P \rightarrow F$ transfer cross sections.	68
VIII. Values of $Q'(nF)$ needed to satisfy branching ratios and $Q'(nD)$	71

LIST OF FIGURES

Figure	Page
1. The vacuum system	7
2. Arrangement of the experimental apparatus	8
3. The one cm beam electron gun.	11
4. The optical system.	16
5. Apparent cross sections of states cascading to the 2^3P state	23
6. Apparent cross sections of states cascading to the 2^1P state	24
7. Apparent cross sections of the 2^3P state.	27
8. Cascade correction to 2^3P at low energy	29
9. Corrected cross section of the 2^3P state.	30
10. Pressure dependence of $Q'(2^1P)$ and $Q_c(2^1P)$	32
11. Values of the right-hand side of Eq. (29) for different pressures	33
12. Apparent cross sections of the 2^1P state.	35
13. Corrected cross section of the 2^1P state.	37
14. Graph of $Q(2^1P) E$ versus E	41
15. Cascade correction to 2^3S apparent cross section.	44
16. Energy level diagram of helium.	45
17. Pressure dependence of the D states	52
18. Pressure dependence of the 1P states.	53
19. Spectrum of F state radiation	54

LIST OF FIGURES (Cont'd.)

	Page
20. Apparent cross sections of the 4^1P and $4F$ states versus pressure	61
21. Apparent cross section of the $4F$ state	63
22. The vacuum furnace	77
23. The high temperature electron gun.	80
24. Beam current versus retarding potential curve.	81
25. Faraday cage temperature versus furnace current.	83
26. Intensity of 4438 \AA line versus pressure	86
27. Ground state density versus temperature.	87
28. Apparent cross section of the 3^3D state versus temperature.	89
29. Apparent cross section of the 4^3D state versus temperature.	90
30. Apparent cross section of the 4^1P state versus temperature.	91
31. The 4^1P to $4F$ transfer cross section versus temperature.	96

CHAPTER I

INTRODUCTION

This paper is intended to describe the experimental methods and analysis of data that lead to values for excitation cross sections of certain states of the helium atom. In some cases, the excitation is produced by the collision of a ground state atom with an already excited atom, leading to an excitation transfer. In other cases, we are interested only in excitation produced by electron impact. These two modes of excitation are measured in terms of the transfer cross section or electron excitation cross section respectively. Other methods of populating excited states include cascading (radiative transitions) from other states and absorption of resonance radiation. The fundamental experimental measure of the populating processes is determined by a measurement of the photon emission rate from a particular excited state and is called the apparent cross section for excitation to that state. If the photon rate can be measured absolutely by comparison against a standard source the cross section so obtained is called an absolute apparent cross section. The population gain and loss rates from the excited state may then be equated and information obtained on the population process. We shall also be concerned with the variation of the apparent cross

section with the energy of the incident electron. In view of the importance of the apparent cross section, a brief derivation follows.

Consider a gas which contains N ground state molecules per cm^3 . If we project a steady beam of electrons along x through the gas and suppose that each molecule offers a cross sectional area for collision of $Q \text{ cm}^2$, then the total target area in a segment of thickness dx in a beam of cross sectional area A will be $NQAdx$. The probability for collision between an infinitesimal electron and a gas molecule is thus

$$dP = \frac{NQAdx}{A} \quad . \quad (1)$$

The probability that an electron will undergo a collision at x is also proportional to the ratio of the number colliding per sec in dx at x to the total number passing through dx per sec so that

$$dP = - \frac{dI(x)}{I(x)} \quad (2)$$

using Eq. (1) we then have

$$Qdx = - \frac{I}{N} \frac{dI(x)}{I(x)} \quad . \quad (3)$$

One usually observes a segment of the beam from x_1 to x_2 .

Integration of Eq. (3) over these limits yields

$$I_2 = I_1 e^{-QN(x_2-x_1)} \approx I_1 [1 - QN(x_2-x_1)] \quad (4)$$

$$QN(x_2-x_1) \gg \frac{1}{2} [QN(x_2-x_1)]^2 \quad (5)$$

The expression for the collision cross section is thus

$$Q = \frac{I_1 - I_2}{(x_2 - x_1) I_1 N} = \frac{\Delta I}{\Delta x I_1 N} \quad (6)$$

Here I_1 is the number of electrons per sec entering the region of observation where ΔI electrons per sec collide.

We now consider inelastic collisions whereby an excited state k is produced. We use the word state in a broad sense to include any group of closely spaced states which are not optically resolved. Under steady state conditions the number of photons $I_p(k)$ emitted from state k per sec will be equal to the number of atoms excited to state k per sec. These in turn are equal to the number of colliding electrons per sec leading to the excitation. Equation (6) can then be written as

$$Q'(k) N \Delta x \frac{I}{e} = I_p(k) \quad (7)$$

where I/e is the beam current divided by the electronic charge. Equation (7) defines only the apparent cross section, $Q'(k)$, for excitation to state k since in general there are processes other than electron excitation which may contribute to $I_p(k)$. In many cases one can observe only photons corresponding to one of several transitions from state k . Denoting this rate by $I_p(k \rightarrow j)$ we have

$$Q'(k) N \Delta x \frac{I}{e} = B(k \rightarrow j) I_p(k \rightarrow j) \quad (8)$$

where the branching ratio $B(k \rightarrow j)$ is defined by

$$B(k \rightarrow j) = \frac{I_p(k)}{I_p(k \rightarrow j)} \quad (9)$$

If one is dealing with a system possessing cylindrical symmetry, and $N(k,R)$ is the density of atoms in state k at radial distance R in the vicinity of a beam of current density $j(R)$, then Eq. (8) becomes

$$Q'(k) \frac{N}{e} \Delta x \int_{-\infty}^{\infty} j(R) R dR = \Delta x B(k \rightarrow j) A(k \rightarrow j) \int_{-\infty}^{\infty} N(k,R) R dR \quad (10)$$

Here $A(k \rightarrow j)$ is the transition probability per sec for $k \rightarrow j$ emission. For convenience in later equations the integral on the R.H.S. (right-hand side) of Eq. (10) is taken equal to $N(k)S$, where $N(k)$ is some average excited state density and $N(k,R)$ is zero outside some area S . Equation (8) becomes

$$\frac{IN}{eS} Q'(k) = N(k) B(k \rightarrow j) A(k \rightarrow j) . \quad (11)$$

$A(k \rightarrow j)$ for spontaneous dipole transitions have been tabulated by Gabriel and Heddle (1).

CHAPTER II

DESCRIPTION OF EXPERIMENTAL APPARATUS

The Vacuum System

A block diagram of the vacuum system is shown in Fig. 1. The vacuum system is of conventional design with a major advantage of being constructed primarily of stainless steel. This eliminates costly down time for lengthy bake out procedures and also the need for a glass blowing specialist. The system is constructed so that its main portion may be covered by a specially constructed bake-out oven. It may be baked out automatically at a preset temperature (up to 400°C) and for a preset time.

Auxillary equipment for pressure measurement includes a large McLeod gauge, a sensitive Pirani gauge, and an automatic scale-changing ionization gauge. These gauges are all of commercial manufacture.

The Optical System

The optical system arrangement is shown in Fig. 2. The lenses employed are of optical grade quartz. The windows in the vacuum system are sapphire. The standard lamp also has a quartz window. The particular monochromator shown in Fig. 2 is a $\frac{1}{4}$ meter focal length Jarrell-Ash. Gratings that are used with this instrument are blazed

at 0.3, 0.6, 1.2, and 2.1 μ . Also a $\frac{1}{2}$ meter Jarrell-Ash with .5 μ blaze grating is used. The latter instrument is superior to the former in the U.V. spectral regions due to its lower light scatter. The $\frac{1}{4}$ meter instrument is useful in the I.R. region and has more light gathering power.

The indicated arrangement of the standard lamp in direct line with the collision chamber and monochromator allows for permanent positioning of all optical components.

The Electronic System

The electronic system is shown in Fig. 2, in block diagram form. The essential features for automatically processing the data and recording the apparent cross section as a function of electron energy are the same as those described in a previous paper (2). A brief account of the operation is as follows.

Photons produced by electron impact in the collision region are focused by a lens on the entrance slit of monochromator. Those corresponding to some $k \rightarrow j$ transition are transmitted and fall on the sensitive surface of a light detector (photomultiplier tube or infrared detector). The signal developed is proportional to the photon rate and is of a square wave form due to the modulation of the electron accelerating voltage. A tunable amplifier set at this modulation frequency reduces the relative noise content of the signal. Further signal to noise improvement is obtained through the use of a phase sensitive detector. This detector rectifies and filters components of the input

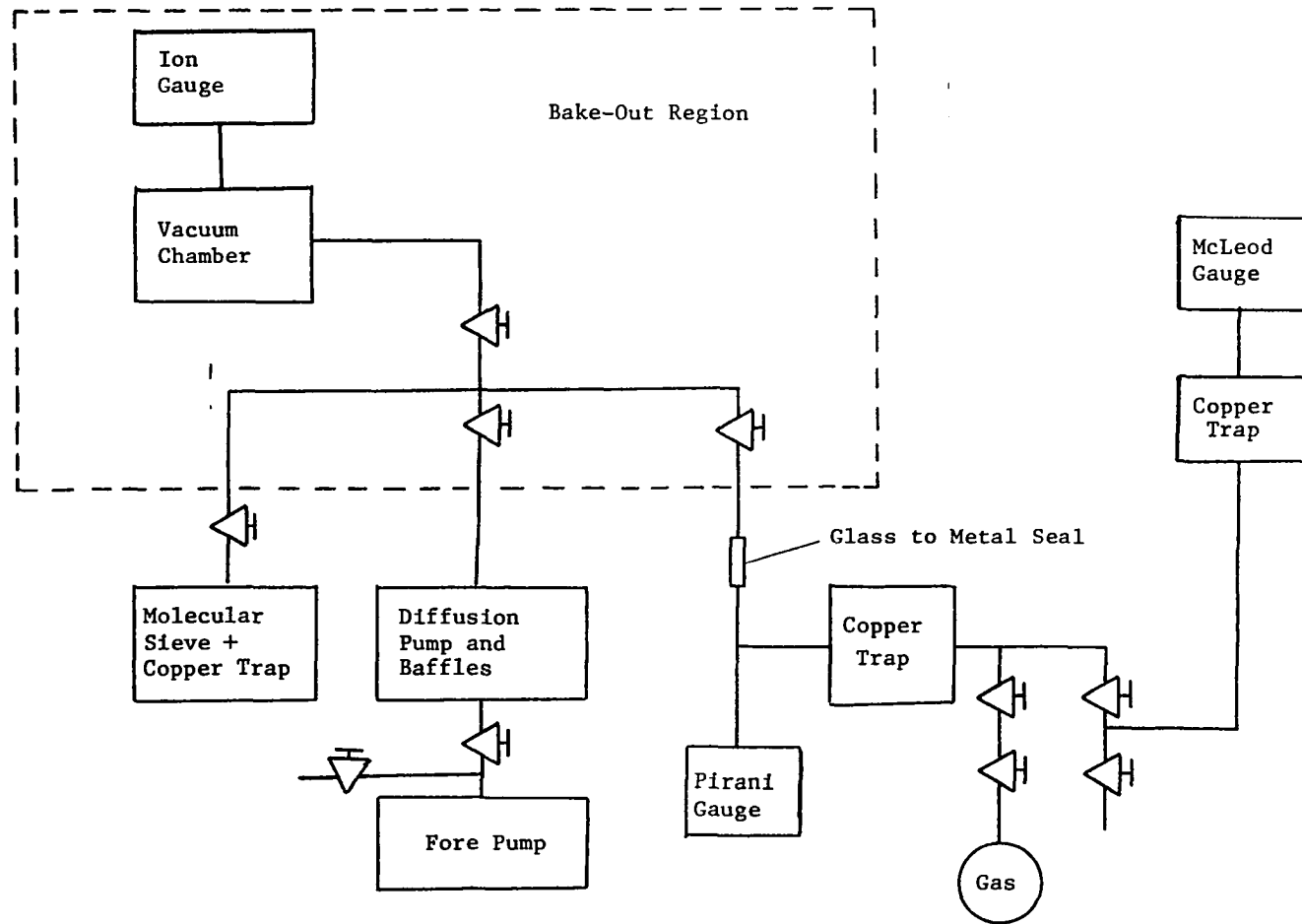


Figure 1. The Vacuum System

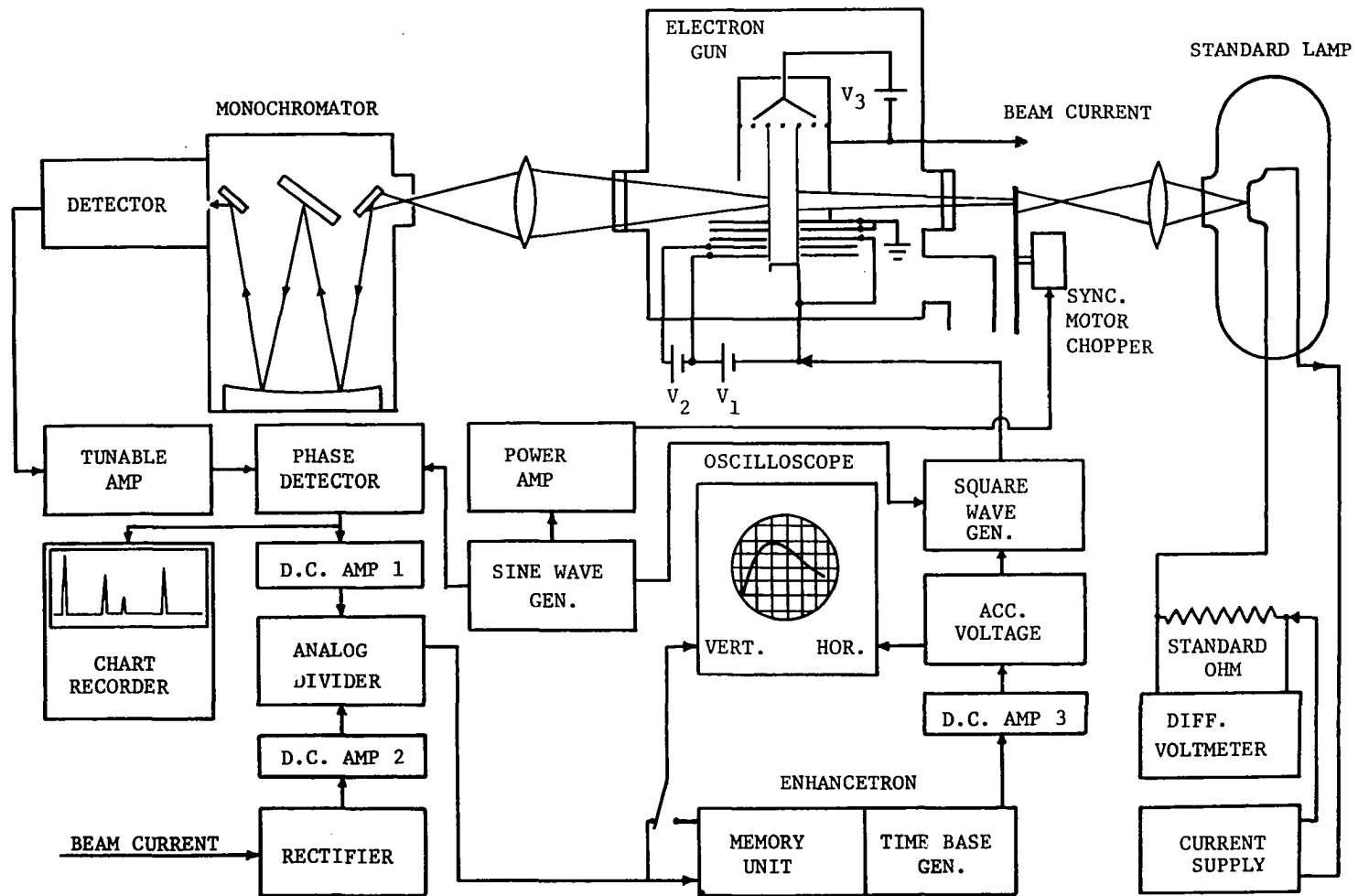


Figure 2. The arrangement of experimental apparatus.

signal which bear a fixed phase relation to a reference source. The detector output is further amplified to a voltage suitable for input to the numerator of an analog divider.

The electron beam current, also of square wave form, develops a voltage across a low resistance which is rectified, amplified, and fed to the denominator of the analog divider. Assuming linearity of the various amplifiers and a constant gas density, the divider output is proportional to the apparent cross section. The output of the divider is connected to the vertical deflection plates of an oscilloscope and the accelerating voltage to the horizontal deflection plates. As the accelerating voltage changes a curve is generated which is termed the optical excitation function. One may also record the excitation spectrum of the gas at constant voltage by slowly rotating the grating of the monochromator.

A major advantage over previous systems is the centrally located sine wave generator. In addition to serving as a reference signal to the phase detector and as a source signal for the square wave generator, the sine wave voltage is amplified by a push-pull amplifier and used to drive a synchronous motor chopper for the standard lamp light. One may set the sine wave generator at any desired frequency between 35 and 100 cps and still have the proper frequency and phase relationships between the beam signal, the standard lamp signal, and the reference signal.

Also shown in Fig. 2 is the arrangement of the standard lamp circuit. A regulated current supply sends current through the standard lamp via a standard ohm. The voltage drop across this resistor is

measured by a sensitive differential voltmeter. This allows the standard lamp current to be measured to 5 significant figures. The temperature of the lamp ribbon as a function of current is obtained from General Electric Company, the lamp manufacturer.

The One Centimeter Beam Electron Gun

Much of the experimental data to be described in subsequent chapters depended on the successful design, construction, and operation of a rather large electron gun producing a one cm diameter beam. This gun, shown in Fig. 3, is basically of pentode design. It employs a Phillips dispenser cathode for electron emission. The first grid is maintained 10-30 V positive with respect to cathode and the second grid 100-200 V positive with respect to cathode. The third grid is at cathode potential and serves as a "virtual" cathode. Grid No. 4 is grounded and serves as the final electron accelerating source when the cathode and third grid are raised to the desired negative potential above ground. Grid No. 5 is also at ground and serves to prevent divergent electrons from entering the collision chamber. The collision chamber is grounded through a low resistance current measuring device. The screened anode is biased 22 V positive with respect to the collision chamber and serves to trap secondary electrons.

The grid plates are machined from 304 stainless steel and the collision chamber is formed from the same material. Spacing insulators for the grids are 4 mm diam. pyrex spheres seated in under-sized holes drilled to the correct size for proper grid spacing. All grid plates

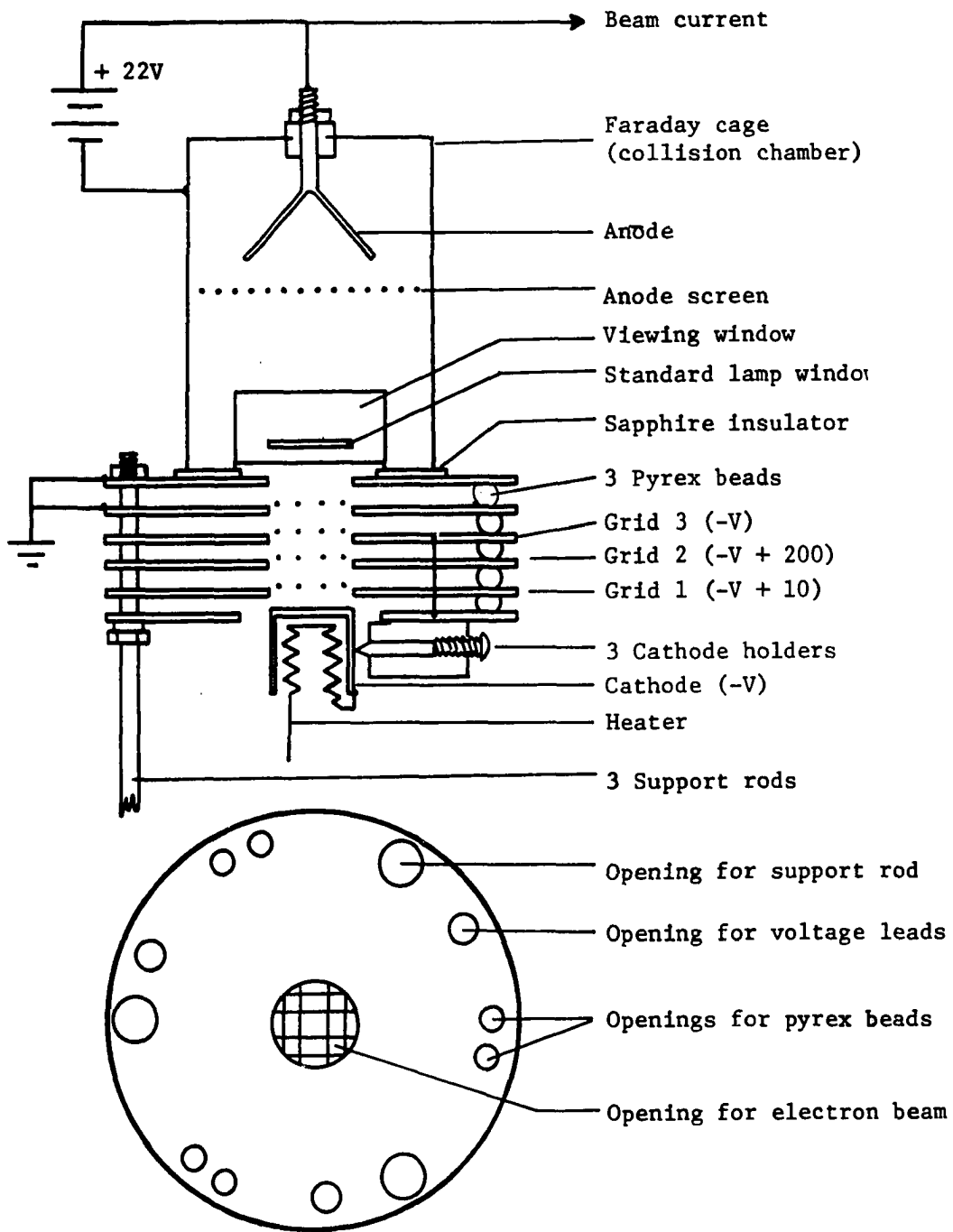


Figure 3. The one cm diameter beam electron gun.

have centrally aligned 1 cm diam. openings. Grid structures are formed over these openings using 8 crossed 0.01" diam, wires. Four wires form an inscribed square and the remaining four are woven and spot welded in such a manner as to form 9 smaller squares. The grid wires are tungsten except for the first grid which is made of nickel wire. The anode screen is gold plated and the anode face is also gold. The cathode is mounted using tungsten tipped stainless steel screws.

The gun shows good pentode characteristics which depend in various degrees on the pressure and type of gas in which it operates.

Although designed primarily for high currents, the good energy resolution of this gun approaches that of guns designed for resolution, these latter types giving currents 100-500 times smaller.

CHAPTER III
MEASUREMENT OF EXPERIMENTAL PARAMETERS

Standardization

The branching ratios in Eq. (8) are obtained from theoretical calculations. The other quantities must be measured experimentally. The measurements of N , Δx , and I in general offer no great difficulty. The main problem is in obtaining an accurate value for the photon rate from the excitation region. This is done by calibrating the detection system with a known photon rate from a standard lamp.

If photons of wavelength λ_0 emitted in solid angle Ω_B are gathered by the optical system, they will generate a signal from the detector given by I_B which is proportional to the photon rate. The constant of proportionality, $E(\lambda_0)$, is termed the efficiency of the detection system. This allows us to write for the photons originating in the electron beam and having isotropic angular dependence

$$\frac{\Omega_B}{4\pi} I_p(k \rightarrow j) = E(\lambda_0) I_B \quad . \quad (12)$$

We now introduce a quantity $P_{\Delta\lambda}$ which is the photon rate into unit solid angle radiated by unit area of a tungsten ribbon and transmitted by a monochromator of triangular band pass of half width $\Delta\lambda$. If such photons from solid angle Ω_{SL} and source area A_0 are collected by

the detection system, we have for the corresponding detector signal I_{SL} that

$$\Omega_{SL} A_o P_{\Delta\lambda} = E(\lambda_o) I_{SL} . \quad (13)$$

Eliminating $E(\lambda_o)$ between Eqs. (12), (13) we have

$$I_p(k \rightarrow j) = 4\pi \frac{I_B \Omega_{SL} A_o P}{I_{SL} \Omega_B} \quad (14)$$

Values for $P_{\Delta\lambda}$ are calculated in the following manner. The photon flux from the tungsten ribbon at temperature T may be considered to be constant over a small wavelength interval $2\Delta\lambda$. This flux may be calculated from Planck's law and the emissivity of the surface. The amount of radiation transmitted by the monochromator is then obtained by integration over its relative transmission function which is defined as

$$T(\lambda) = 1 + \frac{\lambda - \lambda_o}{\Delta\lambda} \quad \lambda_o - \Delta\lambda \leq \lambda < \lambda_o \quad (15)$$

$$T(\lambda) = 1 - \frac{\lambda - \lambda_o}{\Delta\lambda} \quad \lambda_o \leq \lambda \leq \lambda_o + \Delta\lambda \quad (16)$$

We may then write

$$P_{\Delta\lambda} \approx \frac{2 c e(\lambda_o, T)}{\lambda_o^4 (e^{c_2/\lambda_o T} - 1)} \Delta\lambda \quad \text{where} \quad \int_{\lambda_o - \Delta\lambda}^{\lambda_o + \Delta\lambda} T(\lambda) d\lambda = \Delta\lambda \quad (17)$$

Here c is the velocity of light, $e(\lambda_o, T)$ is the emissivity of tungsten, and c_2 is the second radiation constant. The above approximation is very good for $\Delta\lambda < 100 \text{ \AA}$ if $T < 3000 \text{ }^\circ\text{K}$ and $\lambda_o > 2200 \text{ \AA}$. A

1st order correction to $P_{\Delta\lambda}$ is derived by West (3). Values of P_{16} for $\Delta\lambda = 16 \text{ \AA}$ have been calculated by the author on an IBM 1410 computer for a temperature range of 1400 → 3000 °K in increments of 200 °K. The values of λ_0 used in the calculation run from 0.22 μ to 0.70 μ in increments of 0.002 μ and from 0.70 μ to 3.03 μ in increments of 0.010 μ . The emissivity curves of DeVos (4) were digitized by a linear interpolation program for use in the above calculation.

The monochromator pass band $\Delta\lambda$ depends upon equal entrance and exit slit widths s in the following manner.

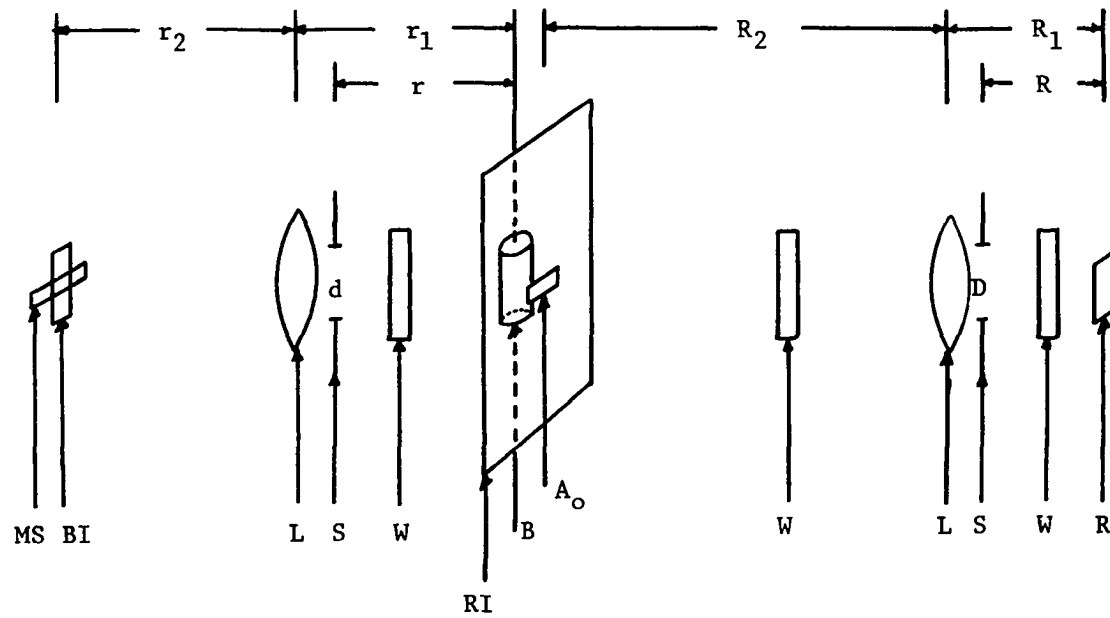
$$\Delta\lambda = \frac{s}{f} \frac{d\lambda}{d\theta} = \frac{s \cos\theta}{fN_g} \quad (18)$$

Here f is the focal length of the monochromator primary mirror and θ the angle between the normal to the grating and the direction of the exit slit. N_g is the ruling density of the grating. In terms of P_{16} we have

$$P_{\Delta\lambda} = \frac{s}{fN_g 16\text{\AA}} \cos\theta P_{16} \quad (19)$$

In order to determine the effective area A_0 of the standard lamp ribbon, an image of the ribbon is focused on a screen inside the Faraday cage of the electron gun just behind the electron beam. This screen is provided with a horizontal slot of precisely measured area A_1 . All light through this slot is allowed to pass into the monochromator. If R_1 and R_2 are the object and image distances of the standard lamp lens, as shown in Fig. 4, then

$$A_0 = A_1 \frac{R_1^2}{R_2^2} \quad (20)$$



MS - Monochromator slit
 BI - Beam image
 L - Lens
 W - Window

B - Beam
 RI - Ribbon image
 R - Tungsten ribbon
 d, D - Stop diameters

Figure 4. The optical system.

Similarly, if the image of the center of the electron beam (which is well defined by the luminosity of excited atoms) is focused on the entrance slit, we have to a good approximation

$$\Delta x = s \frac{r_1}{r_2} \quad (21)$$

where r_1 , r_2 are the object and image distance, respectively, of the beam focusing lens. Moreover, if D and d denote the diameters of limiting stops at distances of R and r from their respective sources, we also have

$$\frac{\Omega_{SL}}{\Omega_B} = \frac{D^2/R^2}{d^2/r^2} \quad (22)$$

When Eqs. (19), (20) and (22) are substituted into Eq. (14) and the result substituted into Eq. (8) along with Eq. (21), we obtain for the final form of the apparent cross section in terms of fundamental quantities

$$Q'(k) = \frac{B(k \rightarrow j) I_B P_{16} \cos \theta}{NI I_{SL}} \left[\frac{e 4\pi D^2 r^2 r_2 R_1^2 A_1}{d^2 R^2 r_1 R_2^2 f N_g 16 A} \right] \quad (23)$$

In some cases, a correction to $Q'(k)$ must be made due to the anisotropy of the radiation $I_p(k \rightarrow j)$. The derivation of the correction term is given in Ref. 5 and consists of a multiplicative factor $(1 - P/300)$ where P is the percentage polarization of the emitted radiation measured at 90° to the beam direction.

General Experimental Procedure

After checking for radiation produced by background gas, a desired amount of gas is introduced into the vacuum chamber. The pressure is read on a McLeod gauge and continuously monitored on a Pirani gauge. N is determined from the pressure by the general gas law. Control experiments are then run and consist of the following:

Linearity check of I_B vs d^2

Linearity check of I_B vs I

Linearity check of I_B vs N

Linearity check of I_B vs s

Control experiments with the standard lamp consists of

Linearity check of I_{SL} vs D^2

Linearity check of I_{SL} vs s

The detection system is then calibrated by obtaining I_{SL} over the desired wavelength range at several different temperatures. Although the ratio of $P_{16} \cos\theta$ to I_{SL} should be constant at all standard lamp temperatures, some deviation is noticed, especially at low temperatures. Some of the deviation can be ascribed to light scattering in the monochromator and can be eliminated by properly chosen broad band pass filters. The procedure adopted in this experiment was to use an average value of the above ratio over the higher temperatures, where the deviation was approximately ± 4 per cent for a change of I_{SL} by a factor of 5.

Shortly after calibration of the detection system, a scan of the spectral lines is made at constant N and I . This yields I_B and when combined with the other parameters in Eq. (23) yields $Q'(k)$. The optical path of the photons from the beam is first adjusted to agree with that of photons from the standard lamp by placing in front of the beam plates of quartz and sapphire. These are of the proper thickness to simulate the rear window of the vacuum system, the standard lamp lens, and the standard lamp window.

CHAPTER IV

ABSOLUTE MEASUREMENTS OF THE 2^1P AND 2^3P ELECTRON EXCITATION CROSS SECTIONS OF HELIUM ATOMS

Description of the Experiment

Up to the present time, no absolute measurements on the cross sections of these lowest lying P states of helium have been available. This is mainly due to the fact that the transitions from these states lie in spectral regions where standard detection techniques are rather insensitive. This chapter is concerned with the experimental methods and analysis of data that lead to absolute values for the electron excitation cross sections of the 2^1P and 2^3P states. For reference purposes, an energy level diagram of helium is presented at the end of this chapter.

For the 2^1P and 2^3P states the transitions which were optically observed were the $2^1P \rightarrow 2^1S$ radiation at 20582 \AA and the $2^3P \rightarrow 2^3S$ radiation at 10832 \AA . In order to measure this radiation a Kodak Ektron type N lead sulfide detector was used. The dimensions of the sensitive area were $0.1 \times 1.0 \text{ cm}$. This detector has a time constant of approximately 500 microseconds and was operated at $25 \text{ }^\circ\text{C}$. The apparatus used to measure the apparent cross sections is the same as shown in Fig. 2. An additional device was used in this experiment to average the excitation functions automatically. This device, a Nuclear Data Model ND-800

Enhancetron, samples the divider output at 1024 equally spaced increments during the accelerating voltage sweep and stores this information in its memory unit. On each successive voltage sweep the corresponding divider outputs are added to those previously stored. The additive nature of the storage significantly reduces random noise.

The $\frac{1}{4}$ meter Jarrell-Ash monochromator with a 2.1μ blaze grating was used for the infrared radiation while the $\frac{1}{2}$ meter monochromator with a $.5\mu$ blaze grating was used for detection of the radiation emitted by the cascading states. In conjunction with the $\frac{1}{2}$ meter instrument, EMI 6256B and RCA 7265 photomultiplier tubes were used.

The Cascading States

Existing information concerning the apparent cross sections of those states that cascade to the 2^1P and 2^3P states was not complete enough to allow a detailed cascade analysis of these states at energies near their excitation threshold. For this reason, absolute apparent cross sections for 22 of these states were measured at 27 volts energy and a pressure of 5μ . These values are presented in Table I along with the values of the 2 P states. The 2^1P value here is corrected for imprisonment. The spectral lines marked * are unresolved. The 7^1S value is interpolated from the 6^1S and 8^1S and used as a correction on the total transition to obtain the 5^3D value.

The excitation functions for these states are presented in Figs. 5 and 6. The vertical scale for each function is fixed by its value at 27 volts given in Table I. The 5^3D function contains

contributions of about 10 → 20 per cent from the 7^1S . Smit, Heidman, and Smit (6) have reported near threshold excitation functions for 11 of these states. The shape agreement is good if one allows for their slightly better energy resolution. It is estimated from the curves of these workers that the halfwidth energy spread of our beam at 5μ is in the 0.4 to 0.5 eV range. This is quite good since the beam currents used for this data were 2 to 5×10^{-3} amp.

Oscillograms of each family of cascading states were obtained by a multiple exposure technique, the monochromator being adjusted to the proper wavelength between exposures. The energy scale for each family is measured relative to the 2^3P onset, which was taken at its spectroscopic value of 21.0 eV. When this is done, all other onsets appear very nearly at their corresponding spectroscopic values.

An interesting phenomenon occurs in the excitation region which the author has termed the "rainbow" effect. This is easily visible only with large electron beams of good energy resolution and is due to the potential gradient along the beam of approximately 2 volts/cm. Owing to the spacing of the energy levels in helium threshold excitation of these levels occurs selectively along the beam. One observes in order of increasing excitation the radiation 6678 and 5876 Å (reddish-yellow) from $n = 3$ states, 5048 through 4471 Å (greenish-blue) from $n = 4$ states, and 4438 Å and lower (bluish-violet) from $n = 5$ and higher levels.

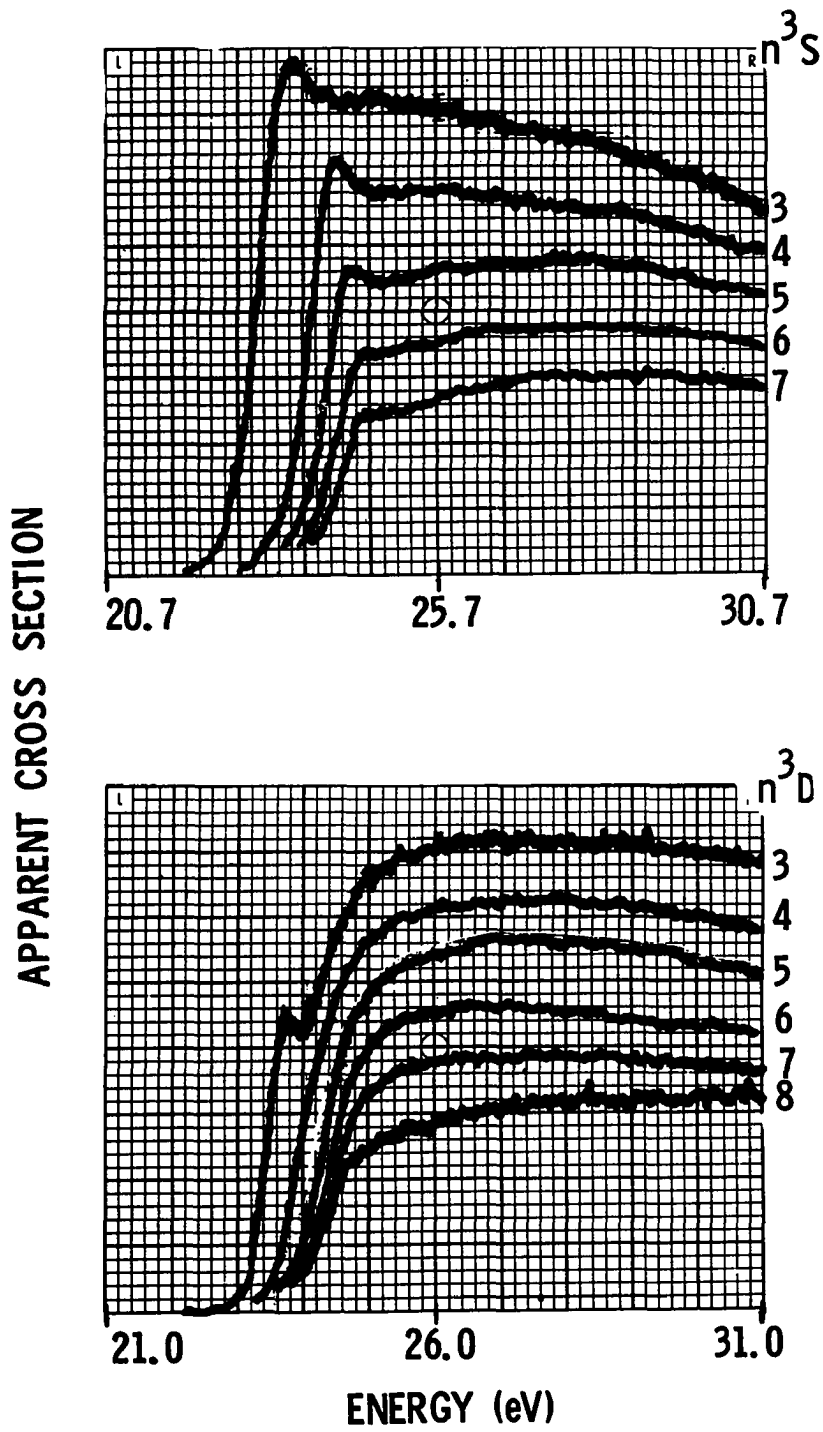


Figure 5. Apparent cross sections of states cascading to the 2^3P state.

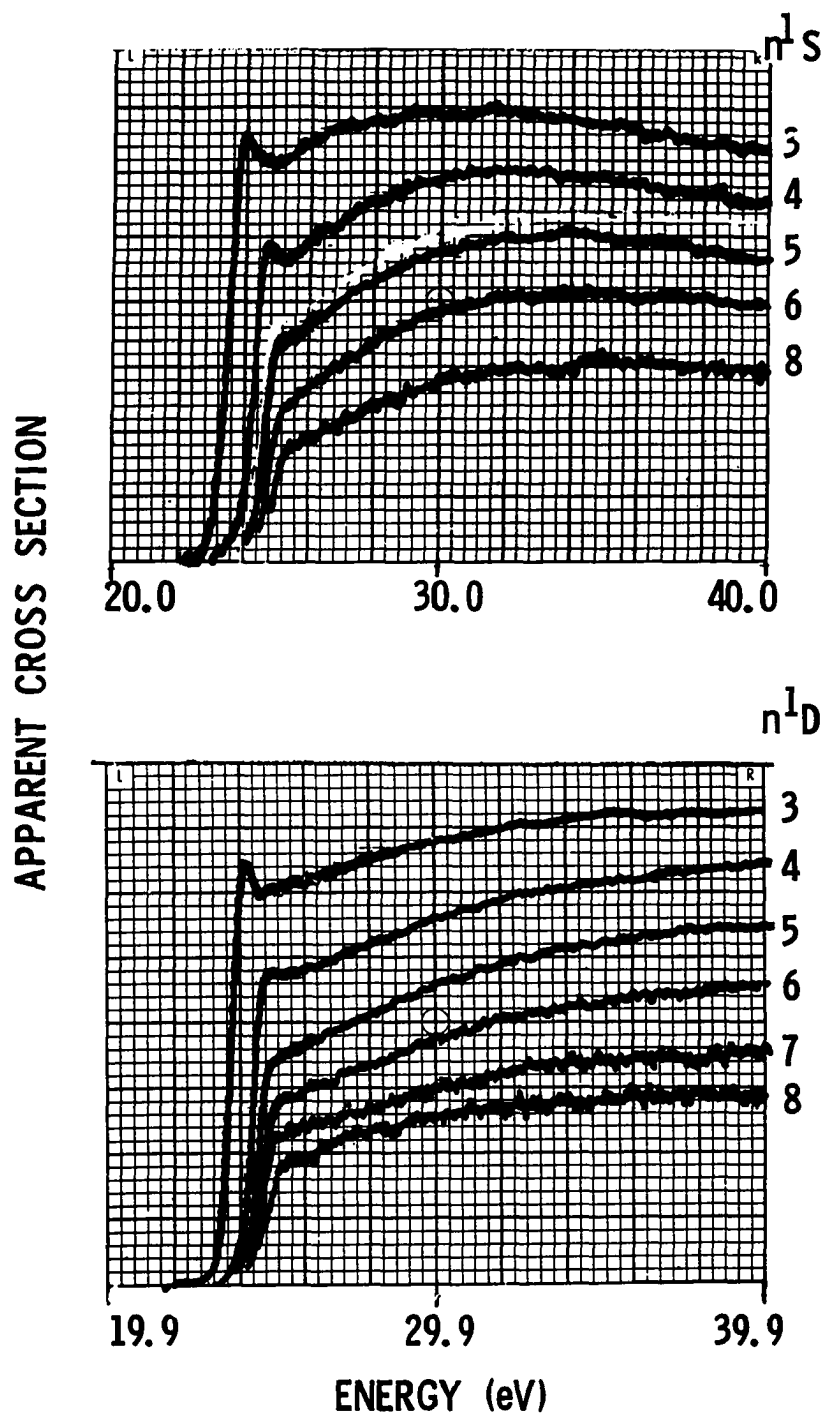


Figure 6. Apparent cross sections of states cascading to the 2^1P state.

Table I. Absolute Apparent Cross Sections of the 2^1P and 2^3P States and Cascading States.

Transition observed (\AA)	Initial State	Apparent Cross Section (10^{-20} cm^2)	
		<u>27 eV</u>	<u>Maximum</u>
20582	2^1P	286	1020
10832	2^3P	400	400
7281	3^1S	56	58
7065	3^3S	95	107
6678	3^1D	32	36
5876	3^3D	32	32
4922	4^1D	14	19
4713	4^3S	32	35
4471	4^3D	14	14
4438	5^1S	9.4	11
4387	5^1D	7.6	11
4169	6^1S	5.0	6.3
4144	6^1D	4.2	5.9
4121	5^3S	15	16
*4026	5^3D	7.5	7.5
*4025	7^1S	2.9	3.8
4009	7^1D	2.2	3.1
3937	8^1S	1.8	2.5
3926	8^1D	1.6	2.2
3867	6^3S	8.5	8.5
3820	6^3D	5.0	5.0
3733	7^3S	5.0	5.2
3705	7^3D	3.3	3.3
3634	8^3D	2.1	2.2

Analysis of DataThe 2³P State

The equation relating the steady state population gain and loss rates per unit volume for the 2³P state can be written as

$$Q(2^3P) \frac{IN}{eS} + \sum_{n=3}^{\infty} [N(n^3S)A(n^3S \rightarrow 2^3P) + N(n^3D)A(n^3D \rightarrow 2^3P)] = N(2^3P)A(2^3P \rightarrow 2^3S) \quad (24)$$

Direct Electron
Excitation

Cascade

Radiative Loss

From Eq. (9) one sees that the branching ratio may be written

$$B(k \rightarrow j) = \frac{A(k)}{A(k \rightarrow j)} \quad (25)$$

This equation, along with Eq. (11), allows one to express the population Eq. (24) as

$$Q(2^3P) = Q'(2^3P) - \sum_{n=3}^{\infty} \left[\frac{Q'(n^3S)}{B(n^3S \rightarrow 2^3P)} + \frac{Q'(n^3D)}{B(n^3D \rightarrow 2^3P)} \right] \quad (26)$$

or simply

$$Q(2^3P) = Q'(2^3P) - Q_c(2^3P) \quad (27)$$

where the last term represents the cascading summation.

The apparent cross section for the 2³P state is shown in Fig. 7 for two energy ranges at 5 μ pressure. Both represent averages of 9 separate scans. At 27 eV $Q'(2^3P) = 4.0 \times 10^{-18} \text{ cm}^2$. For the 20 to 30 volt range, the cascade contribution was calculated using the data discussed in the last section. For the unmeasured cascading states

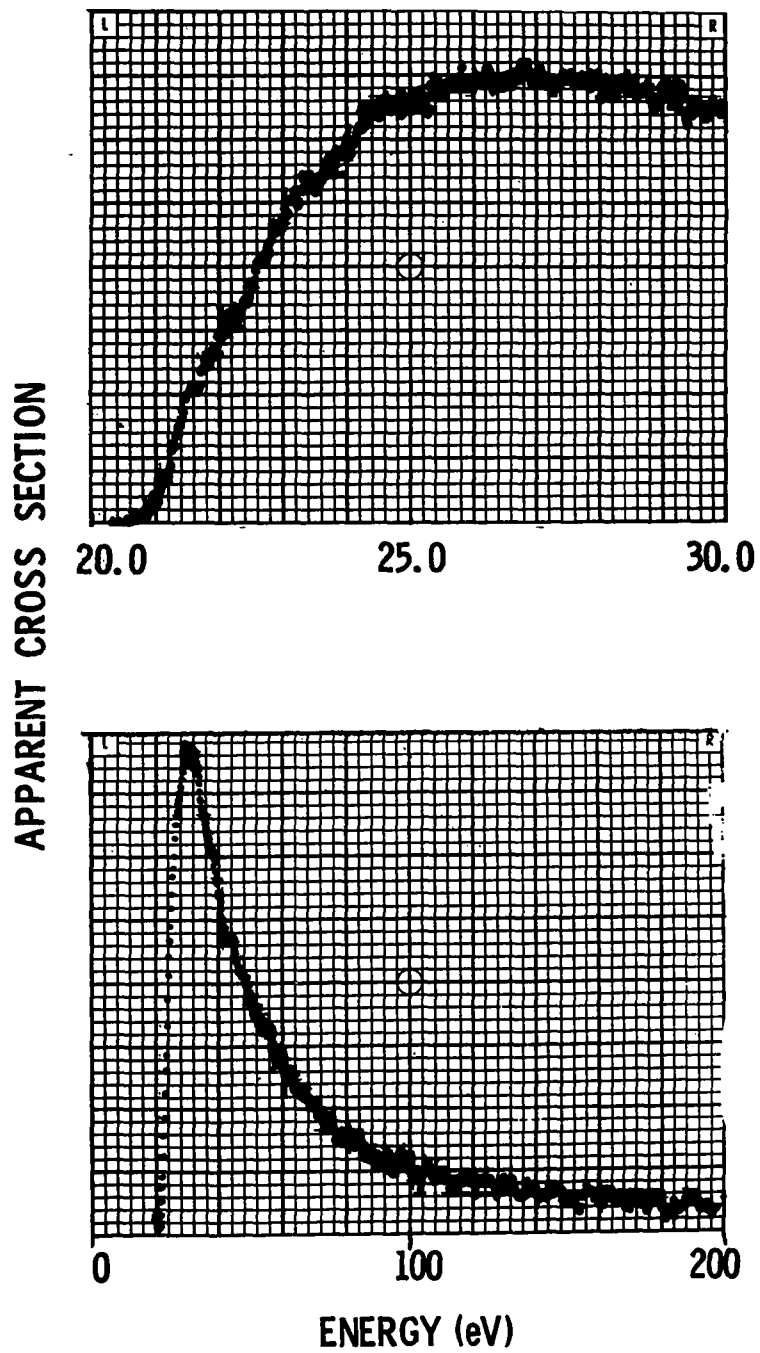


Figure 7. Apparent cross sections of the 2^3P state. Both represent averages of 9 separate scans at 5μ .

($n > 7$ or 8), the small contribution to Q_c (<7%) was determined by extrapolation from a n^{-x} law where x was determined from the data of the lower states. The unmeasured excitation function shapes for high n were assumed to be similar to that of the highest state measured. The curves Q' , Q_c , and Q for the 2^3P state are shown in Fig. 8.

In the higher energy range the shapes of the cascading states are similar and the corresponding corrections to $Q'(2P)$ are simplified. The corrected cross section over the entire energy range investigated is shown in Fig. 9. The x 's on this figure are from the theoretical calculations of Massey and Moiseiwitsch (7).

The 2^1P State

Here we must consider the additional population processes due to the imprisonment of resonance radiation. If we denote by g the fraction of resonance photons that are not absorbed by the gas but escape to the absorbing walls of the collision chamber, then the population equation for the 2^1P state takes the form

$$[Q(2^1P) + Q_c(2^1P)] \frac{IN}{eS} + (1-g)N(2^1P)A(2^1P \rightarrow 1^1S) = \quad (28)$$

$$N(2^1P)[A(2^1P \rightarrow 1^1S) + A(2^1P \rightarrow 2^1S)] .$$

Using the definition of apparent cross section and solving for the quantity of interest we find

$$Q(2^1P) = \frac{Q'(2^1P)}{B(2^1P \rightarrow 2^1S)} \left[g \frac{A(2^1P \rightarrow 1^1S)}{A(2^1P \rightarrow 2^1S)} + 1 \right] - Q_c(2^1P) . \quad (29)$$

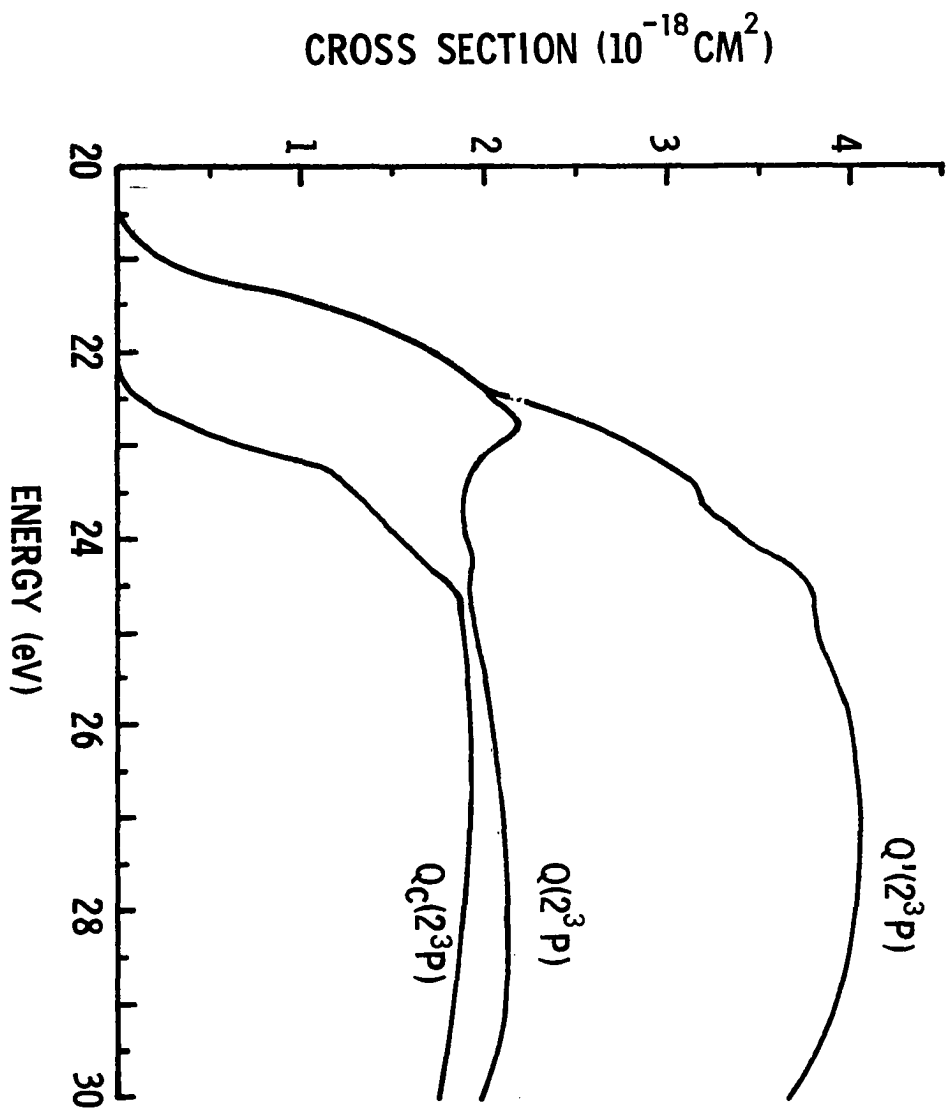


Figure 8, Cascade correction to the 2^3P state at low energy.

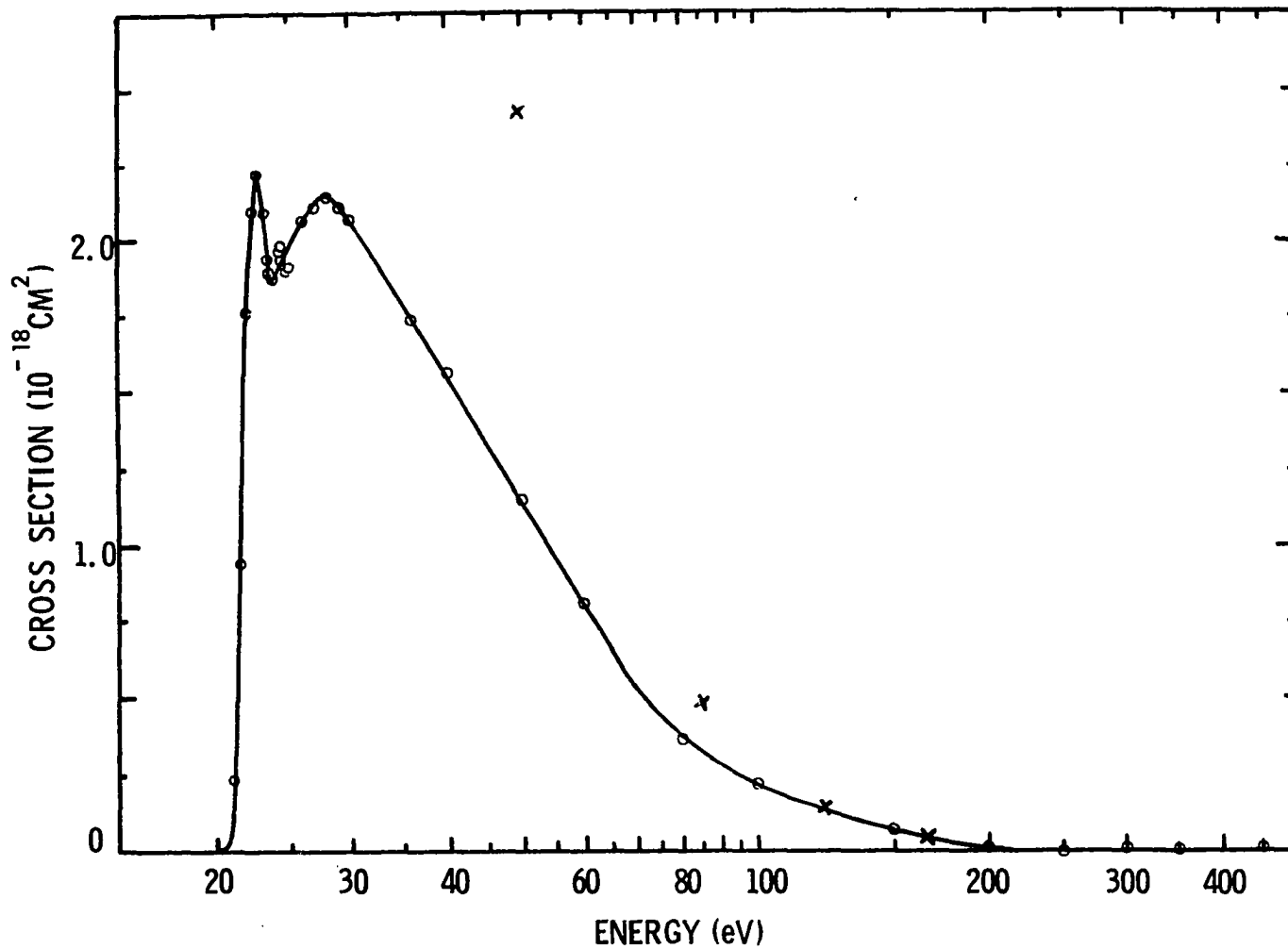


Figure 9. Corrected cross section of the 2^3P state. X - Calculated in Ref. (7).

Limits on the value of g have been obtained by Phelps (8) for a collision chamber of cylindrical symmetry and radius R . From these values one may obtain g as a function of R and the pressure p for a line subject to Doppler broadening only. Gabriel and Heddle (1) have applied the analysis of Phelps in order to obtain the electron excitation cross section of the 3^1P state. One may use a similar analysis to correct for the imprisonment of the 2^1P state since detection of the infrared radiation from this state at pressures low enough to give zero imprisonment is practically impossible. Indeed, even at 1μ pressure, imprisonment is still about 93 per cent.

In practice the collision chamber is usually nearly enclosed at both ends, contains viewing windows, etc., so that one no longer has ideal cylindrical geometry. One must therefore attempt to determine an effective radius ρ . One substitutes different values of p and ρ in the R.H.S. of Eq. (29) to see if there is a unique value for $Q(2^1P)$ at all pressures. The values of $Q'(2^1P)/B(2^1P \rightarrow 2^1S)$ and $Q_c(2^1P)$ are obtained for various pressures from the experimental curves shown in Fig. 10. The quantity $g(\rho, p)$ is evaluated over a range of values of ρ for each pressure with the aid of the graph presented in Ref. 1. The results of this analysis for 100 volt electrons are shown in Fig. 11. Here are presented curves of $Q(2^1P)$ vs. ρ for the three pressures of (a) 60μ , (b) 30μ , and (c) 4.5μ . One sees that for an effective radius of about 0.95 cm we have the solution $Q(2^1P) = 9.2 \times 10^{-18} \text{ cm}^2$. Curves at higher pressures tended to yield lower values of $Q(2^1P)$ but at these pressures effects other than Doppler broadening become important as discussed in Ref. 8.

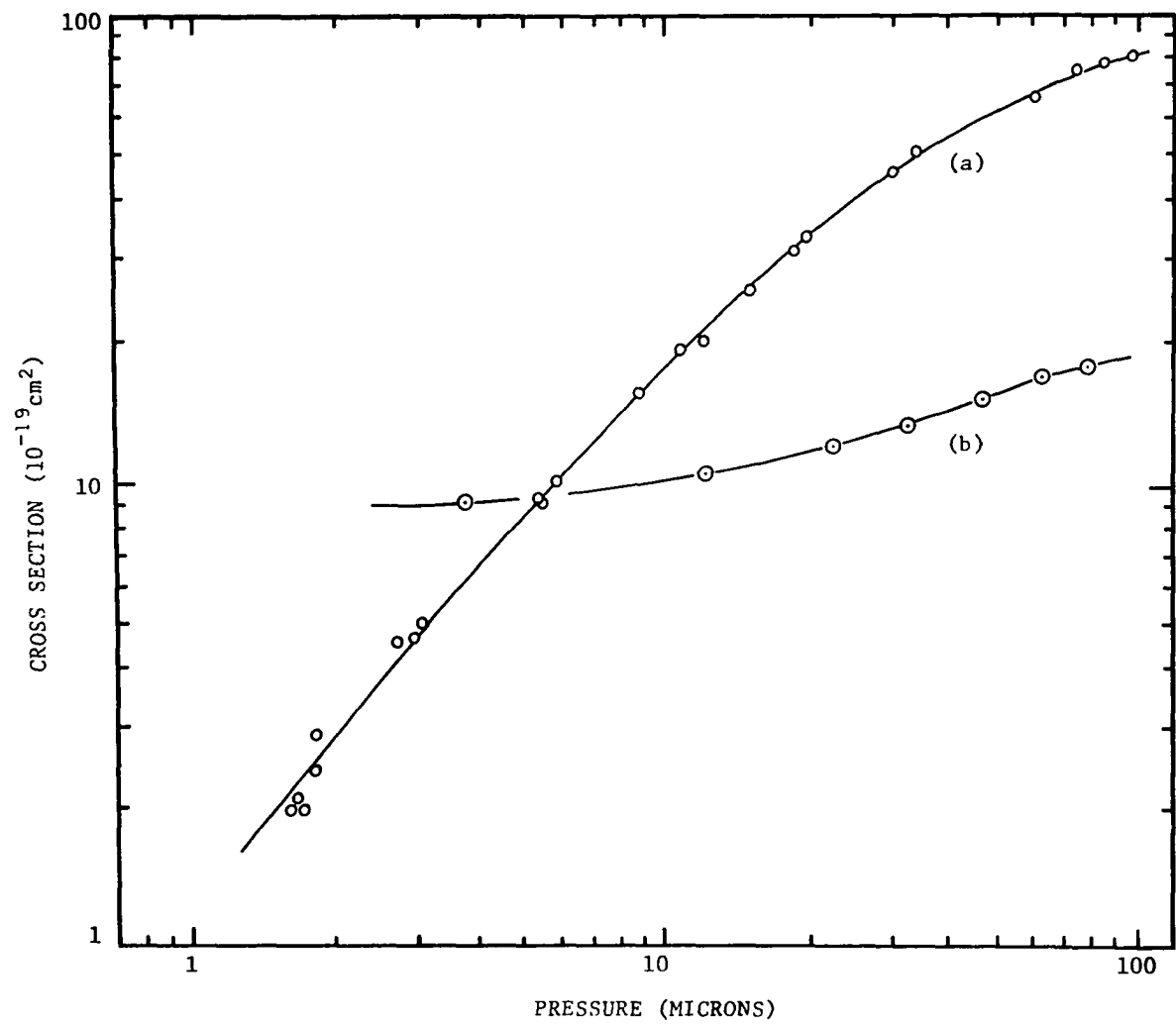


Figure 10. Pressure dependence of (a) - $Q'(2^1P)B^{-1}(2^1P \rightarrow 2^1S)$, and (b) - $Q_c(2^1P)$.

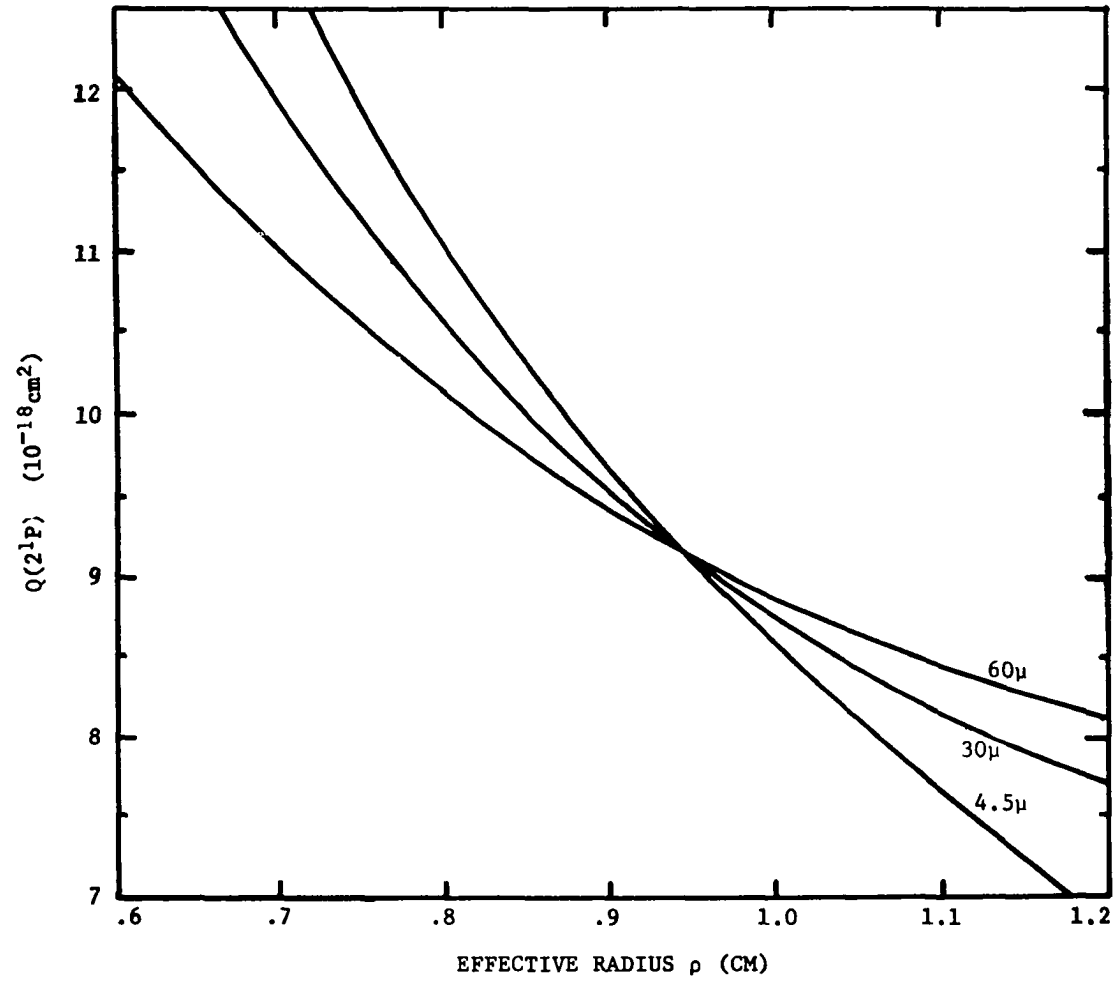


Figure 11. Values of the R. H. S. of Eq. (29) vs. ρ for 3 pressures.

The cross sectional area of the collision region under observation was 0.5 mm in thickness and situated 0.4 cm from the end plate of the collision chamber where the electron beam was admitted. The actual radius of the collision chamber was 1.5 cm but due to the presence of the end plate one would expect the effective radius to lie between 0.4 and 1.5 cm. The calculated value 0.95 cm therefore seems reasonable.

The cascade contribution to the 2^1P state at 100 eV shows pressure dependence due to the enhancement of the 1D series population at high pressures. The 1S series shows little or no pressure dependence. The 2^1P apparent cross section for two energy ranges is shown in Fig. 12. The shape of this function shows little pressure dependence and is typical of other 1P states. The top function represents an average of 25 scans at 4μ pressure and the bottom function is an average over 9 scans at 8μ pressure. Cascade corrections were applied at all energies in the manner described in the last section. The corrected cross section is shown in Fig. 13. On this figure, x represents theoretical values of Massey and Mohr (9) and Δ represents theoretical values of Vainshtein and Dolgov (10).

The apparent cross sections of the 1D series are significantly affected by polarization (up to 12%) and hence were corrected for this effect accordingly by the expression given in Chapter III. The polarization correction for the 3D series has a maximum value of only 4 per cent and hence was neglected.

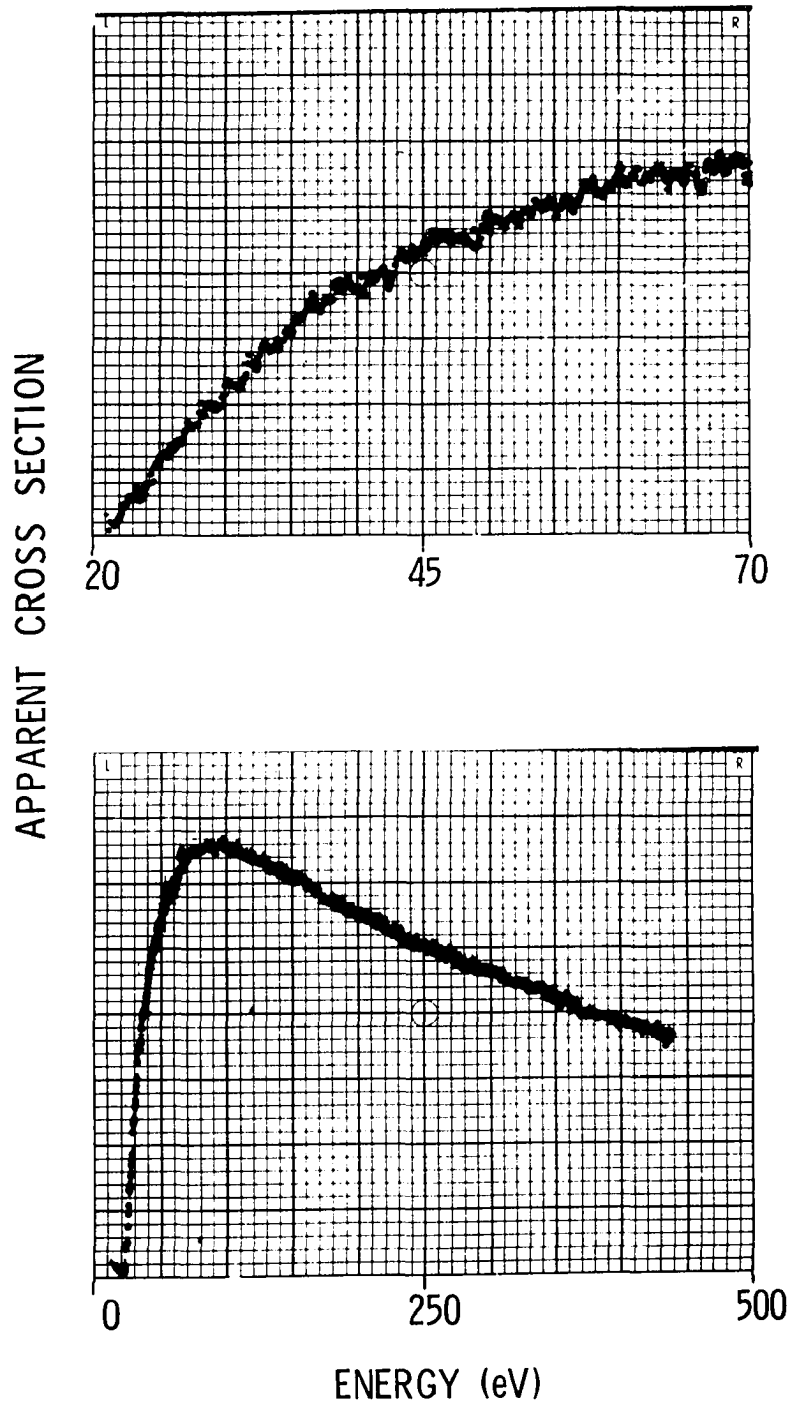


Figure 12. Apparent cross sections of the 2^1P state
 Top: Average of 25 scans at 4μ pressure.
 Bottom: Average of 9 scans at 8μ pressure.

It was not possible to determine exact polarization values for the 2^3P and 2^1P radiation at low pressures due to weak signals. However, by using a Nicol prism, it was determined that the polarization was not more than 10 per cent from onset to 100 eV at 10μ pressure. A polarization value of 10 per cent would imply a correction to the apparent cross section of about 3 per cent.

Discussion of Results

The cross section for the 2^3P state is noticeable for the fact that it approaches zero rapidly at energies beyond 100 eV in complete agreement with the theoretical values. Beyond 200 eV all the apparent cross section can be accounted for by cascade. The exchange distorted wave approximation calculation by Massey and Moiseiwitch (7) gives for the maximum of the 2^3P cross section a value about 6 times the experimental result while their Born-Oppenheimer approximation gives a maximum about 13 times as large. The almost exact agreement at 170 volts must be considered as somewhat fortuitous since the experimental error for this small a value of the cross section is large owing to the fact that cascade correction was 75 per cent of the total apparent cross section. There is apparently a sharp resonance peak close to onset for the 2^3P cross section similar to those observed for some of the apparent cross sections of low n in Figs. 5 and 6.

The result for the 2^1P state is subject to more error than the 2^3P state due to the uncertainty in the correction for imprisonment effects. Hence one must consider the agreement with the Born

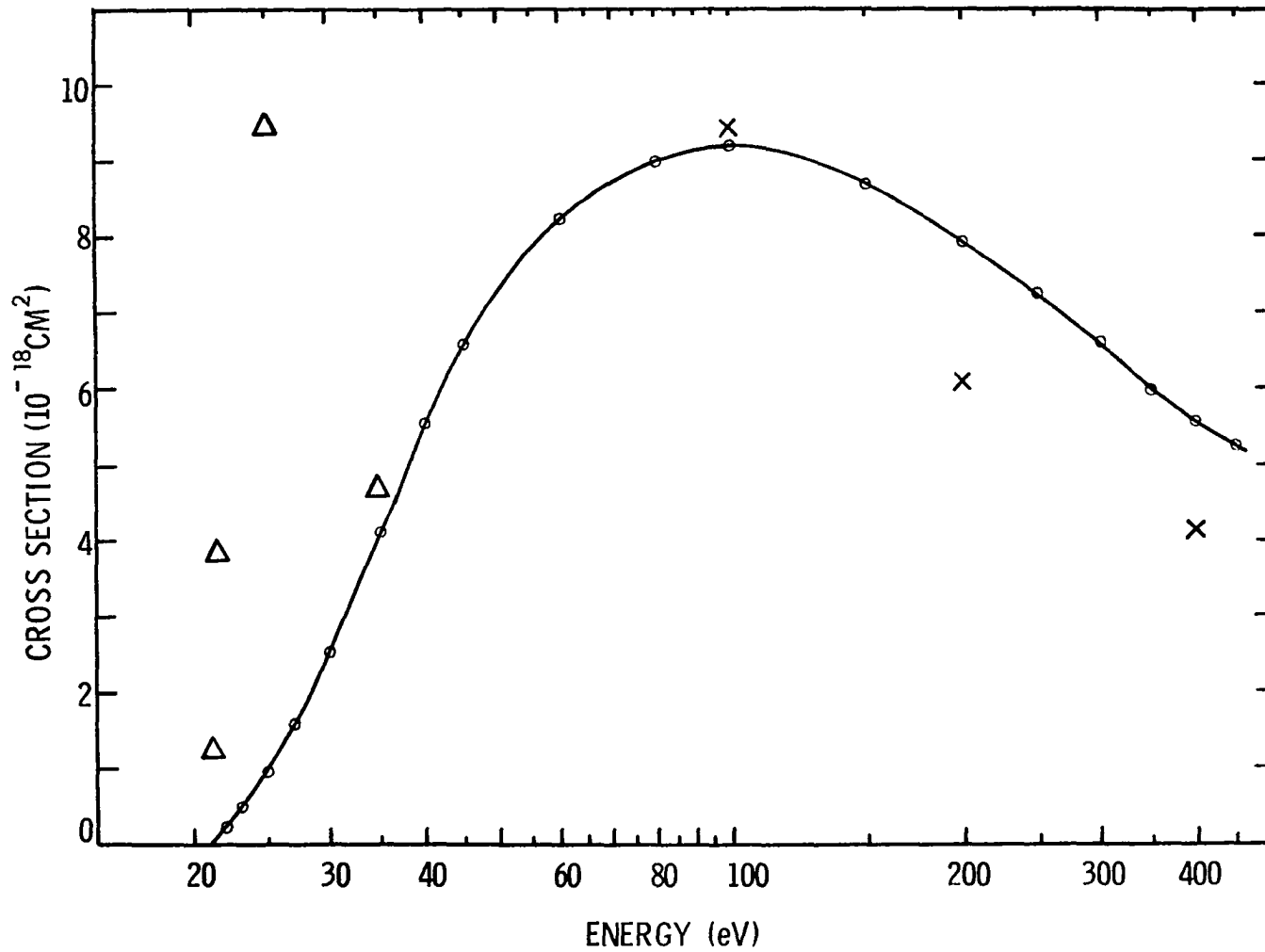


Figure 13. Corrected cross section of the 2^1P state. X, Δ calculated in Ref. (10), (11).

approximation calculation (9) to be quite reasonable. The theoretical results (10) shown for the low energy range however predict more of a triplet shaped function and consequently show poor agreement with the experimental result.

Moussa (11) has studied the 2^1P state by means of its radiation to the ground state at 584 \AA . He estimated a cross section of 870×10^{-20} at 100 eV which is in good agreement with the result obtained here. However, there is poor agreement between the shapes of the excitation functions as Moussa obtained a maximum of $1080 \times 10^{-20} \text{ cm}^2$ at 60 eV and 504×10^{-20} at 400 eV, as compared to $825 \times 10^{-20} \text{ cm}^2$ and 560 cm^2 from Fig. 13.

The apparent cross sections of the S and D states in Figs. 5 and 6 deserve some discussion. There is little doubt that the peaks near threshold for the $n = 3$ states are associated with direct electron excitation since cascade processes start at a slightly higher energy. In particular, the sharp peak on the 3^3D just above threshold is observed to be pressure independent up to 63μ , while the broad maximum doubles in magnitude relative to the sharp peak. The onset of this broad maximum corresponds to that of the $4F$ state, and may be caused by $4F \rightarrow 3^3D$ cascade. Since the cascade analysis of the 2^3P seems to indicate a similar peak due to direct electron excitation, one is tempted to associate some near threshold "resonance" effect to all non-optically allowed excitations. This is not entirely in agreement with theory, as Massey and Moiseiwitsch (7) did not find a 2^3P resonance peak using the exchange distorted wave method, but did find

a 2^3S resonance peak with this method. However, their 2^3S cross section is in good agreement with experiment and the 2^3P value is not.

Applications

One may determine the optical oscillator strength for the 2^1P state from the behavior of the electron excitation cross section at high energies. According to Schram and Vriens (12), within the validity of the Bethe approximation the cross section for excitation to an optically allowed state n is given in terms of the oscillator strength $f(n)$ by the equation

$$Q(n) = \frac{4\pi a_1^2 R^2}{E(n)E} f(n) \ln[c(n)E] . \quad (30)$$

Here a_1 is the Bohr radius, R the Rydberg, $E(n)$ is the excitation potential of state n , E the electron impact energy, and $c(n)$ is a constant which depends upon the shape of the curve expressing the dependence of $f(n)$ on the momentum change of the incident electron. The optical oscillator strength for a transition is defined in terms of the matrix element for dipole transitions as

$$f(n \rightarrow m) = \frac{E(n)}{R a_1^2} |P_{mn}|^2 \quad (31)$$

A graph of $Q(2^1P)E$ versus $\ln E$ should therefore show a straight line at sufficiently high energy with a slope M given by

$$M = \frac{4\pi a_1^2 R^2}{E(2^1P)} f(2^1P) \quad (32)$$

from which the oscillator strength may be calculated.

Such a graph is shown in Fig. 14. One sees that there is a good straight line fit for energies greater than about 80 eV. The slope yields an oscillator strength 0.30. This is compared with experimental values in Table II. Also given are a few of the numerous theoretical values for the 2^1P oscillator strength. The agreement is well within the accuracy of this experimental value.

Holt and Krotov (18) have measured the excitation function for the metastable 2^3S state by using electric field quenching of the 2^1S state. Their function is given in Fig. 15 and shows significant 2^3P cascade effects above 21 eV. The apparent cross section of the 2^3P state obtained in the present work may be used to correct the 2^3S apparent cross section. The energy spread of the beam used by Holt and Krotov is close to the spread of the beam used in the present work. Holt and Krotov have shown that the 2^3S peak at 20.5 eV is affected only a few per cent by unquenched 2^1S . Hence an absolute value of the total metastable cross section at 20.5 eV could be used to fix the ordinate of their curve. The values reported in the literature for the total metastable cross section at the 2^3S peak are 5×10^{-18} , $(4.0 \pm 1.2) \times 10^{-18}$, and $(2.6 \pm 0.4) \times 10^{-18} \text{ cm}^2$ by Maier-Leibnitz (19), Shulz and Fox (20), and Fleming and Higginson (21), respectively. The factor of 2 spread in these values may be reduced by examination of

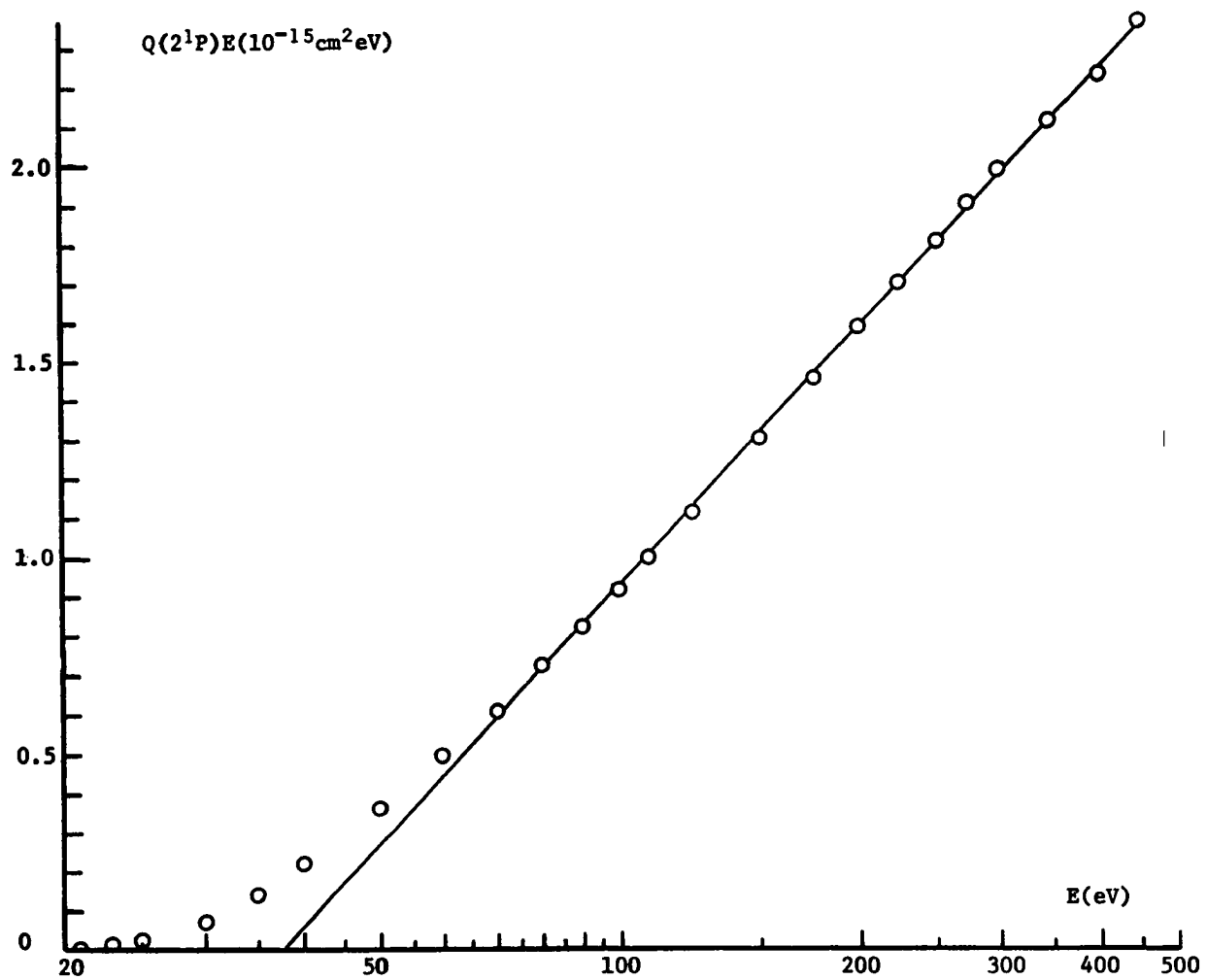


Figure 14. Graph of $Q(2^1P)E$ vs. E

Table II. Experimental and theoretical values of oscillator strengths for 2^1P states.

<u>Experimental</u>	
Skerble and Lassettre (13)	0.268
Geiger (14)	0.312
This work	0.30
<u>Theoretical</u>	
Schiff and Pekeris (15)	0.2762
Mott and Massey (16)	0.280
Ochkur and Brattser (17)	0.280

the corrected $Q'(2^3S)$. In Fig. 15 the 2^3P cascade has been subtracted for a 2^3S peak value of $4.0 \times 10^{-18} \text{ cm}^2$. The value $2.6 \times 10^{-18} \text{ cm}^2$ for the 2^3S peak would cause it to have a zero value at 23 eV. The true peak value may be somewhat higher than 4.0×10^{-18} as a value of $4.2 \times 10^{-18} \text{ cm}^2$ would give $2.2 \times 10^{-18} \text{ cm}^2$ at 22.0 eV, in agreement with the theoretical calculations of Massey and Moiseiwitch (22). A comparison with this theoretical curve at the peak value ($6 \times 10^{-20} \text{ cm}^2$) would not be valid because of the finite energy spread of the electron beam. Shulz and Philbrick (23) measured the production of 2^3S at an angle of 72° by inelastic scattering methods and found at 23 eV a value of 0.21 times the peak value. This would occur in Fig. 15 if the peak value were $3.9 \times 10^{-18} \text{ cm}^2$. Of course one must assume isotopic scattering in this case. It is concluded that the best agreement with theory and experiment for the 2^3S peak at about 0.4 eV energy spread is close to $4.0 \times 10^{-18} \text{ cm}^2$.

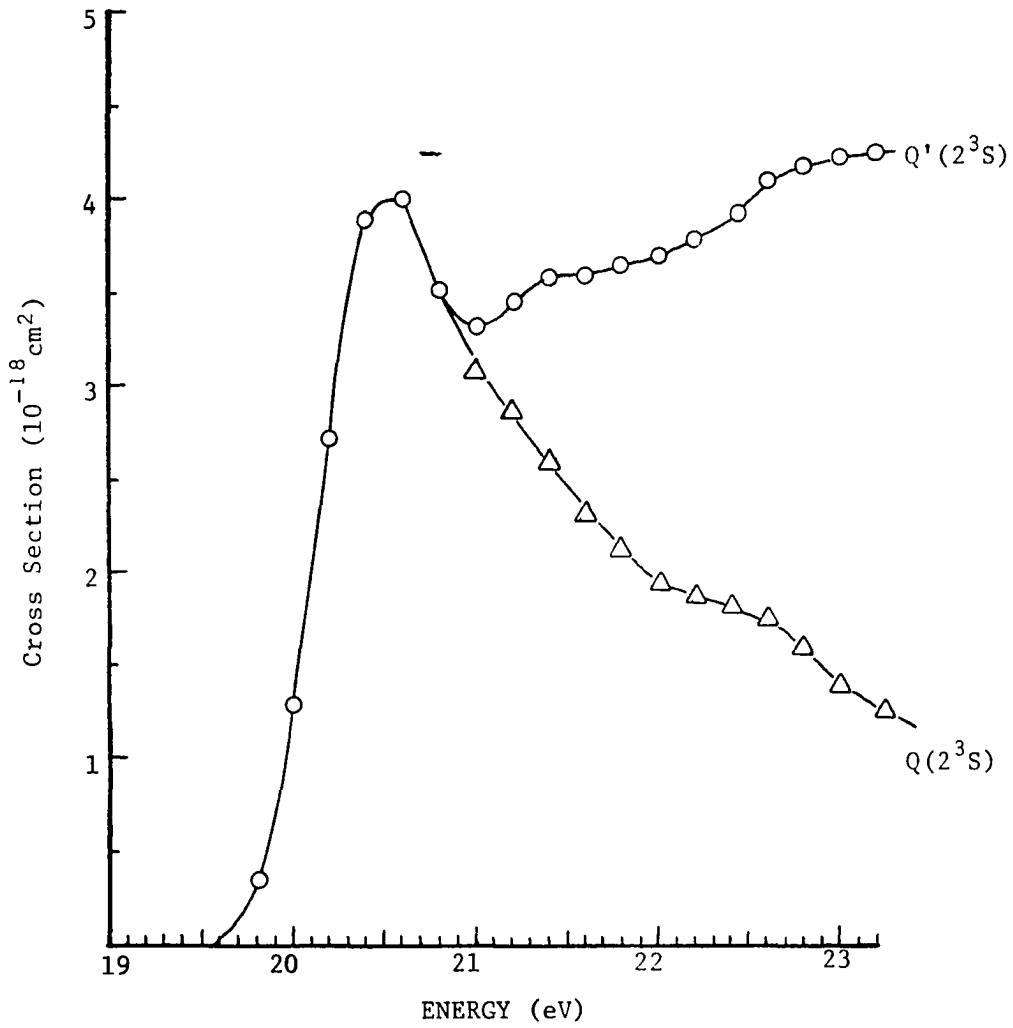


Figure 15. Cascade Correction to 2³S Apparent Cross Section

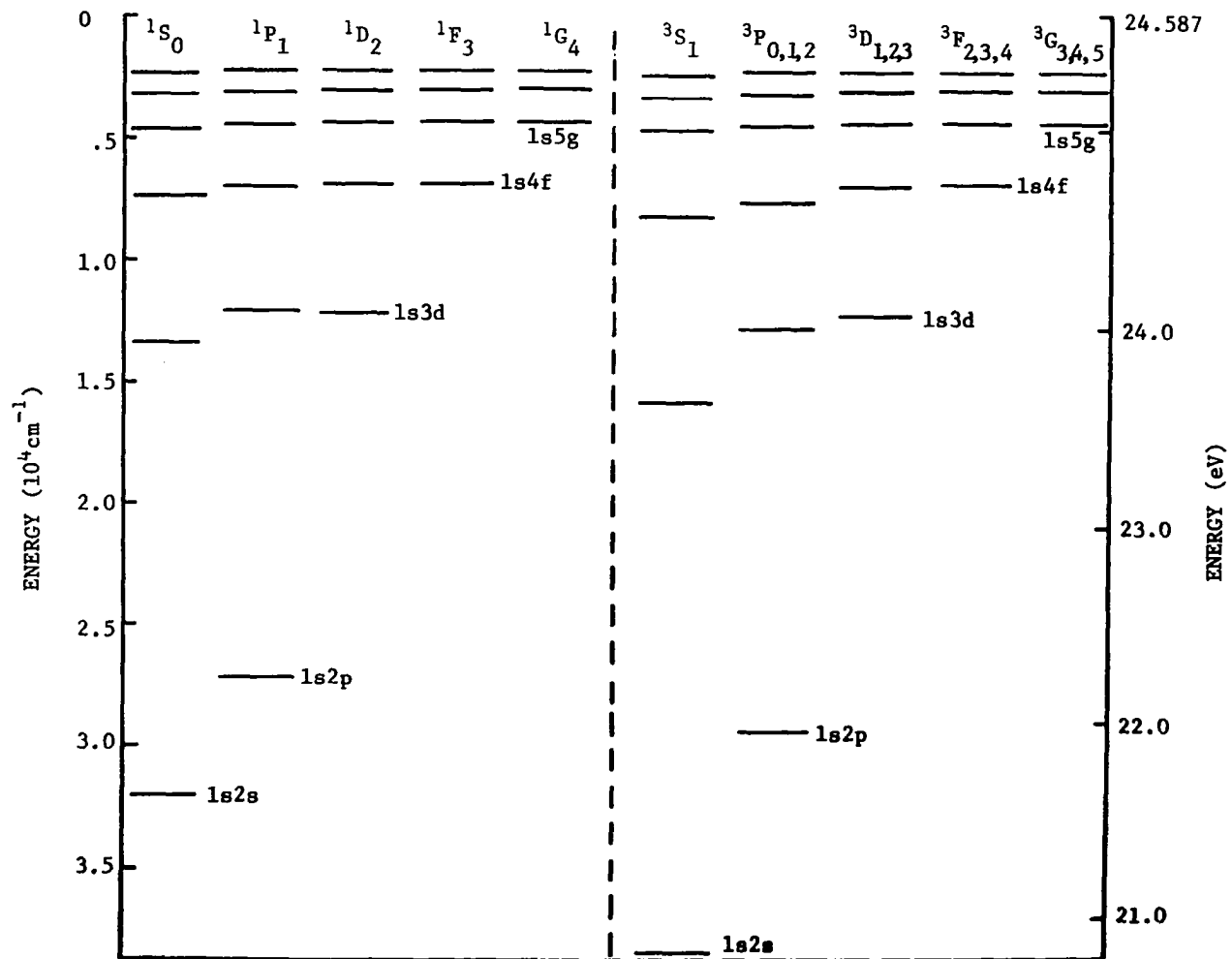


Figure 16. Energy level diagram for excited states of HeI.

CHAPTER V

EXCITATION TRANSFER PROCESSES IN HELIUM

Description of the Experiment

This experiment was undertaken in order to clarify the processes which cause the apparent cross sections of various states to show marked dependence on the ground state density. Interest in the past has centered primarily on the behavior of the low n singlet and triplet D states with pressure. Early researchers (24,25) assumed that the excessively high populations of these states at pressures above a few microns were due to a process whereby a n^1P atom was transferred to a n^1D or n^3D state of excitation by a collision with a ground state atom. While conforming to experimental evidence then available, the transfer cross section for such processes seemed somewhat large. In addition, a $n^1P \rightarrow n^3D$ transition for states with good Russell-Saunders coupling violates the Wigner spin conservation rule. To alleviate these difficulties, a model was introduced by St. John and Fowler (26) in which the n^1P excitation is transferred via a collision with a ground state atom to the nF state. The excess excitation of the D states is then due to F state cascade from many levels. This model yields smaller transfer cross sections and avoids violation of the Wigner spin rule since the total spin of an F state is not well defined.

Energy considerations allow excitation transfer only between states of the same n , unless n is greater than about 12. A theoretical treatment of the problem by Bates (27) shows that the probability for excitation transfer increases as the internal energy difference between initial and final excited states decreases. Excitation transfer effects involving n^3P states are therefore less probable than those involving n^1P states since the energy separation of n^3P and n^3L , n^1L are several times larger than the corresponding n^1P separations. In addition, the n^3P population input at 100 eV and high pressure is primarily due only to 3D cascade whereas the n^1P state excitation is due to both large electron impact cross sections and resonance radiation imprisonment. The n^1S and n^3S states show little or no pressure dependence.

Since the introduction of the "multiple state" mechanism of St. John and Fowler the most important experimental work (28,29) has been confined to observations on radiation from the 3 to 6¹P and from the 3 and 4 singlet and triplet D states. The experimental data to be described here are obtained from observations on the radiation from the following 36 states:

n^1P	$n = 3$ to $n = 10$
n^1D	$n = 3$ to $n = 13$
n^3D	$n = 3$ to $n = 13$
nF	$n = 4$ to $n = 9$

In view of the inequality (5) in Chapter I, one is limited as to the maximum pressure that can be used. Using the ionization cross section of Smith (30) and adding to it the total excitation cross section, one obtains a value of $5.5 \times 10^{-17} \text{ cm}^2$ for the total inelastic cross section at 100 eV. The total excitation cross section was determined using the cross sections of the 2P states as given in Chapter IV along with the unpublished work of St. John, Kassik, and Nee on the other excited levels. Owing to gun construction, $x_2 - x_1 = 0.4 \text{ cm}$ and the error introduced in neglecting higher terms of the expansion in Eq. (4) is $\leq 3\%$ for pressures $\leq 70 \mu$.

Presentation of Data

The P and D States

Absolute values for the apparent cross sections of the P and D states were obtained at 63μ pressure, 8×10^{-3} amp beam current, and 100 eV. At this energy the pressure dependence is maximum. The method of standardization has been described earlier. The 1/2 meter Jarrell-Ash was used with proper filters in conjunction with EMI 6256B and RCA 7265 uncooled photomultiplier tubes. The data is presented in Table III. The branching ratios given in this table are calculated from the transition probabilities given in Ref. 1. Occasionally one finds what appears to be an error in these values. When this is the case, a correction is made by reference to the extensive study of helium transition probabilities by Niles (31). Extrapolation was used for $n > 8$.

Table III. Absolute apparent cross sections at 100 eV, $p = 63\mu$, for 1P and D states. $N(k)$ is number density per 10^{-3} ampere beam current for $S = 0.25\pi \text{ cm}^2$. $B(k \rightarrow j)$ are branching ratios.

Transition $k \rightarrow j$	λ (Å)	$Q^1(k)$ (10^{20} cm^2)	$B(k \rightarrow j)$	$N(k)$ (10^5 cm^{-3})
$3^1D \rightarrow 2^1P$	6678	74.5	1.00	1.9
$4^1D \rightarrow 2^1P$	4922	42.5	1.37	2.6
$5^1D \rightarrow 2^1P$	4387	18.2	1.54	2.1
$6^1D \rightarrow 2^1P$	4144	7.0	1.63	1.5
$7^1D \rightarrow 2^1P$	4009	3.2	1.78	1.1
$8^1D \rightarrow 2^1P$	3926	1.5	1.80	.72
$9^1D \rightarrow 2^1P$	3872	.80	1.78	.59
$10^1D \rightarrow 2^1P$	3834	.42	1.79	.44
$11^1D \rightarrow 2^1P$	3805	.25	1.82	.37
$12^1D \rightarrow 2^1P$	3784	.16	1.85	.29
$13^1D \rightarrow 2^1P$	3768	.10	1.86	.24
$3^3D \rightarrow 2^3P$	5876	54.5	1.00	1.2
$4^3D \rightarrow 2^3P$	4471	24.9	1.27	1.3
$5^3D \rightarrow 2^3P$	4026	19.1	1.40	1.9
$6^3D \rightarrow 2^3P$	3820	13.0	1.50	2.1
$7^3D \rightarrow 2^3P$	3705	7.6	1.58	1.8
$8^3D \rightarrow 2^3P$	3634	4.0	1.59	1.3
$9^3D \rightarrow 2^3P$	3587	2.3	1.60	1.0

Table III Continued

Table III (Cont'd.)

$10^3D \rightarrow 2^3P$	3554	1.2	1.61	.69
$11^3D \rightarrow 2^3P$	3532	.62	1.63	.52
$12^3D \rightarrow 2^3P$	3514	.32	1.65	.35
$13^3D \rightarrow 2^3P$	3500	.18	1.65	.24
$2^1P \rightarrow 2^1S$	20580	6.14×10^5	902.	560.
$3^1P \rightarrow 2^1S$	5016	1.42×10^4	43.7	39.4
$4^1P \rightarrow 2^1S$	3965	2.60×10^3	37.5	16.5
$5^1P \rightarrow 2^1S$	3614	4.50×10^2	34.3	5.5
$6^1P \rightarrow 2^1S$	3448	1.06×10^2	31.4	2.2
$7^1P \rightarrow 2^1S$	3355	40.4	30.7	1.3
$8^1P \rightarrow 2^1S$	3297	20.2	30.6	1.0
$9^1P \rightarrow 2^1S$	3256	11.	30.5	.7
$10^1P \rightarrow 2^1S$	3230	6.	30.4	.5

The pressure variation of the apparent cross sections was then determined by the variation of $I_p(k \rightarrow j)$ with pressure at constant I . This data is presented in Figs. 17 and 18.

The F States

The apparent cross sections of the F states are very difficult to obtain owing to the fact that radiation from these states is in the infrared spectral region. The radiation $4F \rightarrow 3D$ at approximately $18,695 \text{ \AA}$ was measured using the $\frac{1}{4}$ meter Jarrell-Ash monochromator with 2.1μ blaze grating in conjunction with a Kodak Ektron Uncooled lead sulfide detector. It was not possible to resolve the nF radiation into its $n^3F \rightarrow 3^3D$ and $n^1F \rightarrow 3^1D$ components which are separated by $\leq 10 \text{ \AA}$.

The $5F \rightarrow 3D$ radiation at $12,790 \text{ \AA}$ is considerably weaker. It is possible, however, to obtain a reasonable signal from this radiation using a PbS detector cooled to liquid nitrogen temperature. A fellow worker, J. D. Walker, is currently engaged in research with such detectors. The apparent cross section for the $5F$ state in Table IV should only be considered as approximate, as it is based on estimates from preliminary spectra obtained by Mr. Walker.

Values for the apparent cross sections for the higher F states were obtained using a liquid nitrogen cooled RCA 7102 photomultiplier tube. A spectrum showing radiation from these states is presented in Fig. 19. This spectrum was taken with the $\frac{1}{4}$ meter monochromator using a 1.2μ blaze grating. Absolute values for these apparent

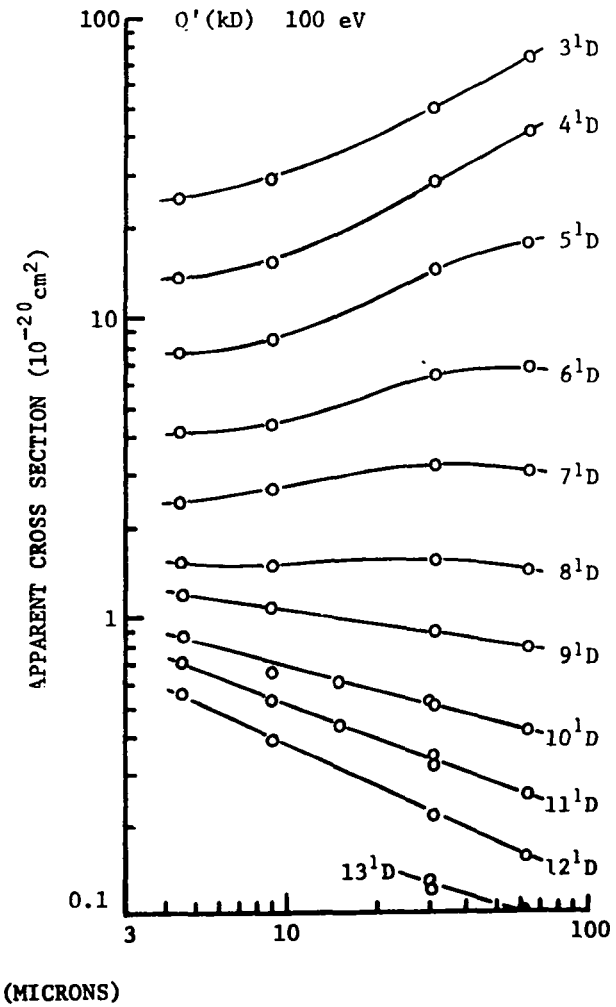
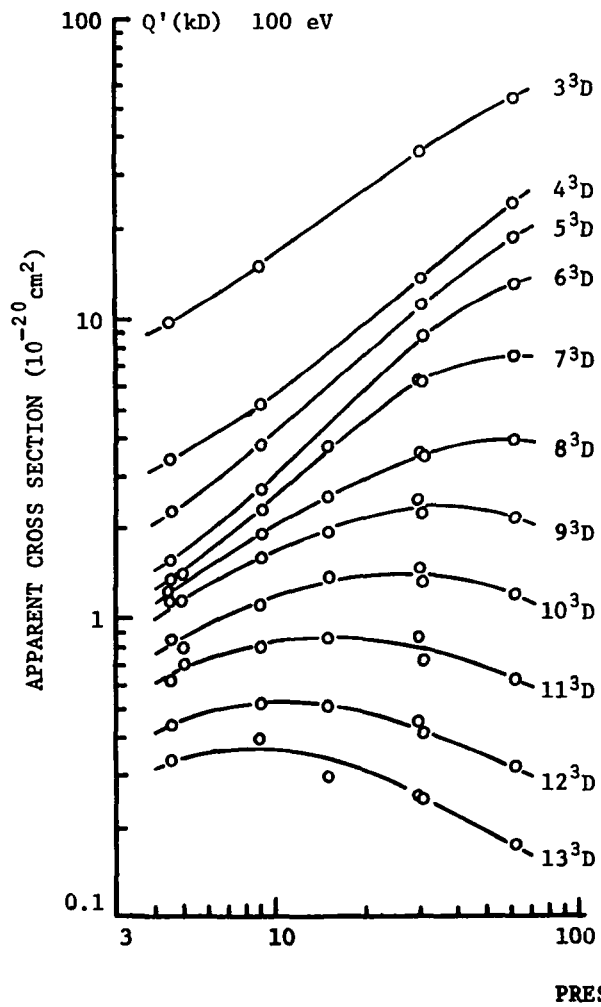


Figure 17. Pressure dependence of the D states.

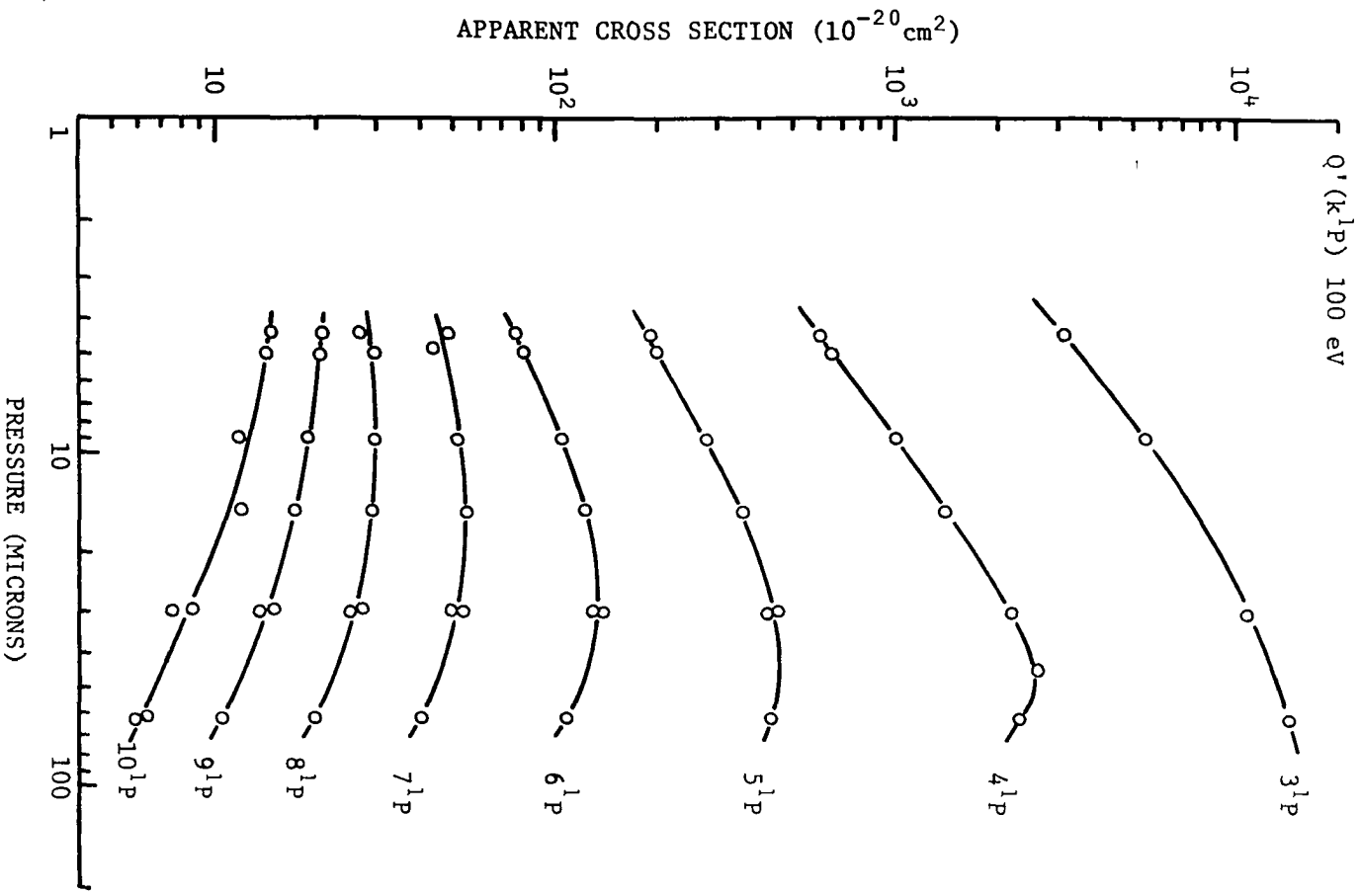


Figure 18. Pressure dependence of the $1p$ states.

TOP SECRET

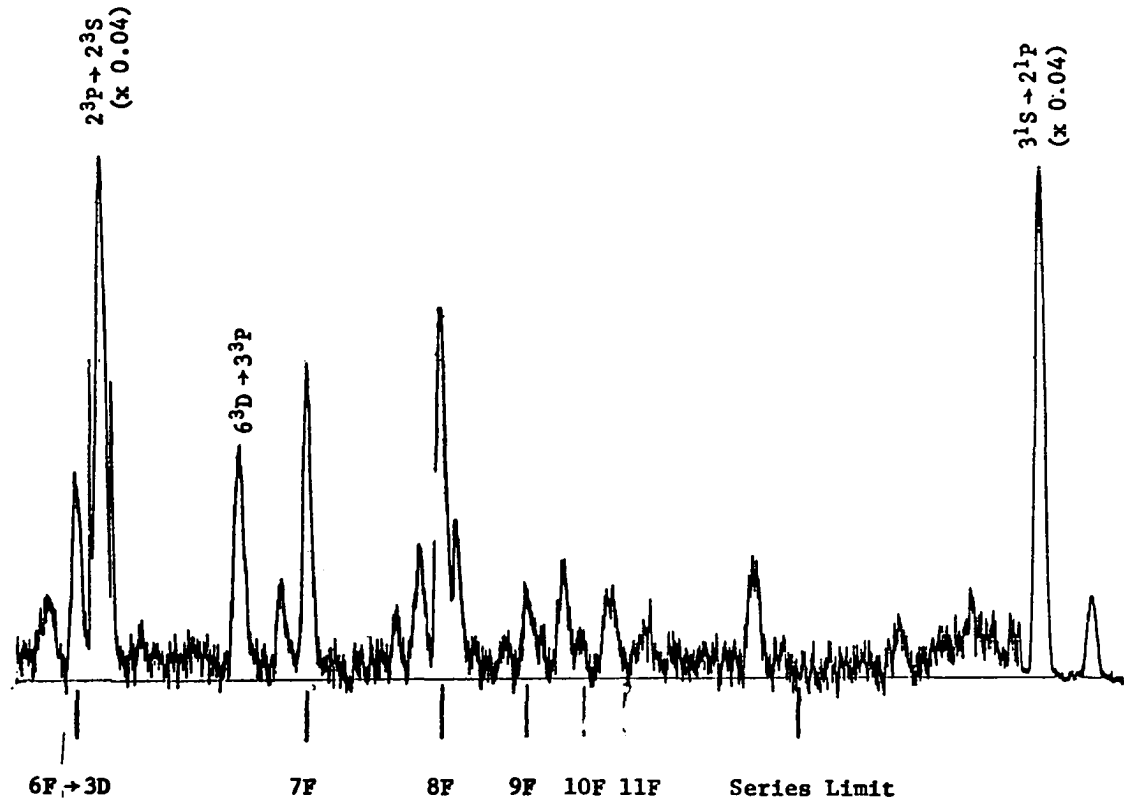


Figure 19. Spectrum at 63μ , 100 eV, showing F state radiation.

cross sections were obtained by comparison with the 3^1S apparent cross section (7281 \AA) and also with the 2^3P apparent cross section ($10,833 \text{ \AA}$) in the following manner. From Eq. (23) we may write for the apparent cross section, denoting the wavelength independent quantities by K ,

$$Q'(k) = K \frac{I_B(\lambda)}{I_{SL}(\lambda)} P_{16}(\lambda) \cos\theta(\lambda) B(k \rightarrow j) \quad (33)$$

$$Q'(k') = K \frac{I_B(\lambda')}{I_{SL}(\lambda')} P_{16}(\lambda') \cos\theta(\lambda') B(k' \rightarrow j') \quad (34)$$

If one has an accurate value of $Q'(k)$, one may eliminate K between these two equations and obtain a value of $Q'(k')$ in terms of $Q'(k)$ and the standardization parameters evaluated at λ and λ' . As a check on $Q'(k')$, one may repeat the procedure using some other known apparent cross section, say $Q'(k'')$.

The $Q'(3^1S)$ and $Q'(2^3P)$ values were used as $Q'(k)$ and $Q'(k')$ and had already been measured in conjunction with the work described in Chapter IV. The results obtained from each of these two lines agreed to within 10 per cent. This should be considered satisfactory in view of the fact that the $10,833 \text{ \AA}$ line was standardized using a PbS detector, the 7281 \AA line standardized on a S-20 response P.M.T., and then both lines compared on a third standardized detector, i.e., the 7102 S-1 response P.M.T.

Radiation from the transitions $nF \rightarrow 3D$ for $n \geq 5$ contains unresolved components. For example, the $n^1P \rightarrow 3^1D$ transitions are $\leq 30 \text{ \AA}$ from the $nF \rightarrow 3D$ lines. However, the populations of the various n^1P

states are known from absolute measurements on the line intensities from these states in the visible. Thus one may calculate the contribution of the $n^1P \rightarrow 3^1D$ components to the total intensity of the unresolved line by using the appropriate branching ratio from the n^1P state. In this way one finds a correction of about 5 per cent for all transitions $nF \rightarrow 3D$, $n = 5$ to 9 , except for $n = 8$. The correction to this line at 9530 \AA is approximately 70 per cent due to $7^3D \rightarrow 3^3P$ radiation. Values of apparent cross sections for the F states are given in Table IV. One notices that the 8F value seems somewhat small. This could in part be due to the uncertainty in the nature of the large correction. The $6^3D \rightarrow 3^3P$ line at $10,314 \text{ \AA}$ is well resolved as can be seen from Fig. 19. The apparent cross section for this line is measured to be $1.92 \times 10^{-20} \text{ cm}^2$. If this were to be predicted from the apparent cross section of the line 3820 \AA , i.e., $B^{-1}(6^3D \rightarrow 2^3P)Q'(6^3D) = 8.7 \times 10^{-20} \text{ cm}^2$, as given in Table III, one would obtain $2.5 \times 10^{-20} \text{ cm}^2$, a value about 30 per cent higher. This is due to the fact that the transition probability ratio (31) $A(6^3D \rightarrow 2^3P)/A(6^3D \rightarrow 3^3P)$ is only 3.5 whereas the measured photon rates from the 6^3D state have a ratio of 4.5. Such errors are not necessarily entirely due to intensity calibration, as can be seen by comparing $A(6^3D \rightarrow 2^3P)$ given in Ref. (31) with the value given in Ref. (1). Fortunately, the corrections to the other F states are small.

Table IV. Apparent cross sections of F states at $p = 63\mu$ and 100 eV. $N(k)$ is for 10^{-3} ampere beam current for $S = 0.25\pi \text{ cm}^2$.

Transition $k \rightarrow j$	λ (Å)	$Q'(k)$ (10^{-20} cm^2)	$B(k \rightarrow j)$	$N(k)$ (10^5 cm^{-3})
4F 3D	18695	69	1.00	8.1
5F 3D	12790	(23)	1.59	5.3
6F 3D	10920	9.2	1.94	3.6
7F 3D	10034	4.2	2.22	2.5
8F 3D	9532	1.2	2.40	1.1
9F 3D	9216	0.9	2.48	1.2

Transition Probabilities from F States

Rather than extrapolate from the few available $F \rightarrow D$ transition probabilities tabulated in Ref. (1), it seemed desirable to calculate as many of these as possible for the higher nF states, particularly in view of the fact that some of these values seemed to be in error. Hydrogenic transition probabilities were calculated since these are a very good approximation to helium transition probabilities for highly excited states of large angular momentum. The hydrogenic transition probabilities were calculated using the confluent hypergeometric series solution of the radial integral as outlined by Condon and Shortley (32). These values show close agreement with recent calculations of nF helium transition probabilities for $n = 4$ to 7 by Wiese and Smith (33) who used the Coulomb approximation of Bates and Damgaard (34).

Calculation of Transfer Cross Sections

The F States

On the basis of the multiple state transfer theory, one may write for the population equation of the nF state

$$Q_{ec}(nF) \frac{IN}{eS} + \bar{v}NN(n^1P)Q_t(n^1P \rightarrow nF) = \bar{v}NN(nF)Q_t(nF \rightarrow n^1P) + N(nF)A(nF) \quad (35)$$

Electron Excitation + Cascade Gain	Transfer Gain	Transfer Loss	Radiative Loss
--	---------------	---------------	----------------

Here $Q_{ec}(nF)$ is the cross section for electron excitation to the nF state and includes possible cascade processes. $Q_t(n^1P \rightarrow nF)$ is the transfer cross section from the n^1P to the nF state. The average relative velocity of the colliding atoms is \bar{v} .

From the principle of detailed balancing we have

$$Q_t(nF \rightarrow n^1P) = \frac{1}{b} e^{-\Delta E/kT} Q_t(n^1P \rightarrow nF) \quad (36)$$

where b is the ratio of the statistical weight of the nF state to that of the n^1P and ΔE is the energy difference of these states. The exponential factor is approximately unity for $n \geq 4$.

One may write Eq. (35) in terms of apparent cross sections by using Eq. (11). Using also Eq. (36) one finds from Eq. (35)

$$Q'(nF) = \frac{\bar{v} N Q_t(n^1P \rightarrow nF) Q'(n^1P) / A(n^1P) + Q_{ec}(nF)}{1 + \bar{v} N Q_t(n^1P \rightarrow nF) / [bA(nF)]} \quad (37)$$

This equation may be used to predict the pressure dependence of $Q'(nF)$. We were only able to obtain a pressure curve for the $4F$ state since signals obtained from the higher nF radiation were very weak at pressures significantly lower than 63μ . The observed pressure variation of $Q'(4F)$ is shown in Fig. 20 along with that of $Q'(4^1P)$.

As the pressure is decreased, the R.H.S. of Eq. (37) approaches $Q_{ec}(4F)$ and $Q'(4F) \approx Q_{ec}(4F)$. Assuming this quantity is constant with pressure, at some high pressure one may solve Eq. (37) for $Q_t(4^1P \rightarrow 4F)$. With these constant values of $Q_{ec}(4F)$ and $Q_t(4^1P \rightarrow 4F)$

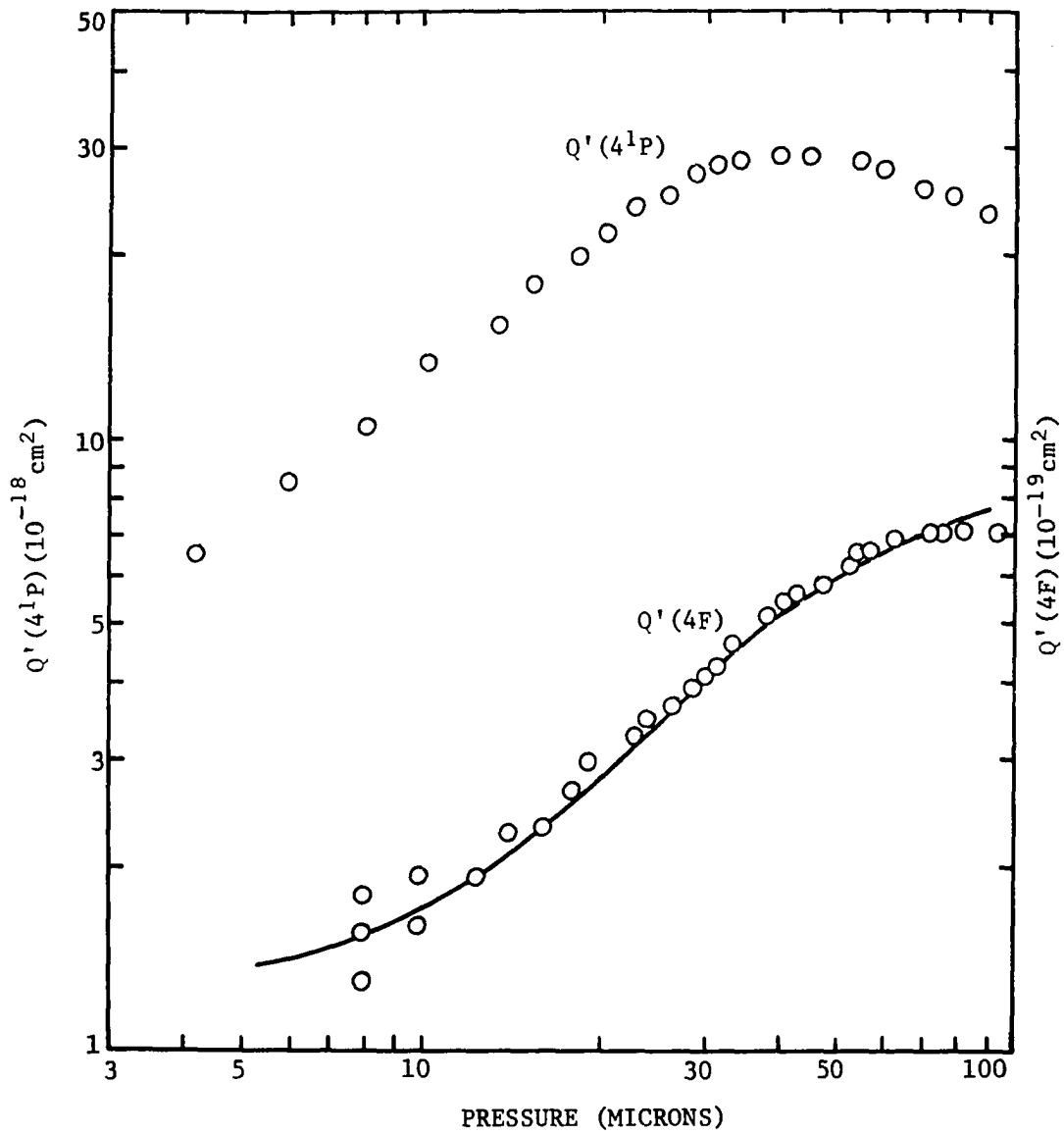


Figure 20. Apparent cross sections of the 4^1P and $4F$ states versus pressure. The solid line is calculated from the right-hand side of Eq. (37).

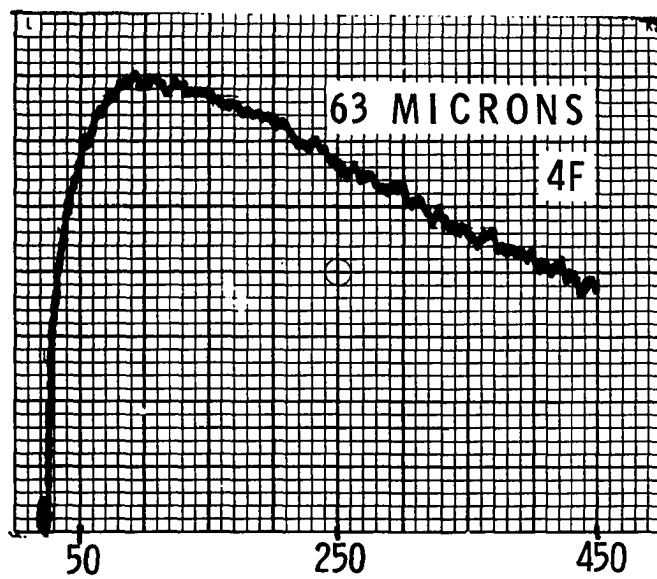
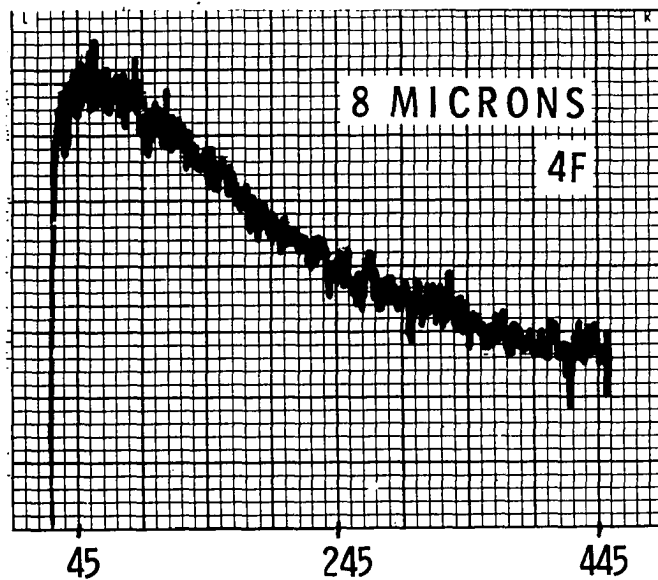
one may predict values $Q'(4F)$ from Eq. (37) at intermediate pressures. These values are also shown in Fig. 20 for $Q_{ec}(4F) = 1.3 \times 10^{-19} \text{ cm}^2$ and $Q_t(4^1P \rightarrow 4F) = 1.5 \times 10^{-14} \text{ cm}^2$.

The value of b depends upon the statistical weight assigned to the $4F$ state. Considering the $4F$ state as a mixture of the singlet and triplet states 1F_3 , 3F_4 , 3F_3 , 3F_2 , and assuming the probability of collisional excitation to any one of these states to be the same, one would obtain $b = 28/3$. If on the other hand the breakdown in Russell-Saunders coupling for the $4F$ state is only partial, the excitation transfer should favor the singlet state to some extent with $b < 28/3$. Kay and Hughes (29) found evidence for the latter case. The value $b = 14/3$ was used in the calculations shown in Fig. 20 since it gave a slightly better fit to the experimental values of $Q'(4F)$ at the higher pressures. The larger value $b = 28/3$ causes a maximum change of only 5 per cent in the denominator of Eq. (37) and only slightly affects the value of $Q_t(4^1P \rightarrow 4F)$.

The excitation function of the $4F$ state shown in Fig. 21 at 63μ pressure closely resembles that of the 4^1P state. This tends to confirm the idea that the dominant populating process of the $4F$ state at this pressure is transfer from the 4^1P state. The shape of the excitation function at 8μ resembles somewhat that of a 1D state.

For the higher nF states Eq. (35) must be considered only as approximate since the possibility exists for excitation transfer to nG , nH , etc., states. Lin and Fowler (35) have shown that the transfer processes under consideration here favor the selection rule $\Delta L = 2$

APPARENT CROSS SECTION



ENERGY (eV)

Figure 21. Apparent cross sections of the 4F state.

so that $5F \rightarrow 5G$ should be small while $6F \rightarrow 6H$ could be considerable. Neglecting such effects, and considering also that $Q_{ec}(nF)$ is small at 63μ pressure, one may obtain approximate values of the ${}^1P \rightarrow F$ transfer cross section from Eq. (37),

$$Q_t(n^1P \rightarrow nF) = \frac{Q'(nF)}{vN} \left[\frac{Q'(n^1P)}{A(n^1P)} - \frac{Q'(nF)}{bA(nF)} \right]^{-1}. \quad (38)$$

These values will be presented later.

The D States

On the basis of the multiple state transfer mechanism, the pressure dependence of the D states can be explained by F state cascade. The population equation for the D states may be written in the same form as Eq. (27) for either the 1D or 3D state separately or both considered as one state.

$$Q'(nD) = Q(nD) + Q_c(nD) \quad (39)$$

where

$$Q_c(nD) = \sum_k [B^{-1}(kP \rightarrow nD)Q'(kP) + B^{-1}(kF \rightarrow nD)Q'(kF)]. \quad (40)$$

The P cascade term is < 5 per cent of $Q'(nD)$. For triplet states the direct electron excitation $Q(n^3D)$ is negligible and for singlet states is obtained from low pressure data on $Q'(n^1D)$. At $P = 63\mu$ and at 100 eV we may use the data from Table IV to obtain the F state cascade. Calculation of the R.H.S. of Eq. (39) in this manner gives

for the $n = 3$ states

$$Q'(3D) = 122 \times 10^{-20} \text{ cm}^2 \quad (41)$$

which is 20 per cent direct excitation, 5 per cent P cascade and 75 per cent F cascade. As given in Table III this quantity was measured using the total radiation from the 3^1D and 3^3D states as

$$Q'(3D) = Q'(3^3D) + Q'(3^1D) = 129 \times 10^{-20} \text{ cm}^2 \quad (42)$$

It is also worthy of note that the nF state radiation measured ended on the 3D level. Hence, excepting the 5 per cent P cascade, the values in Eqs. (41) and (42) primarily represent measured input and output rates of radiation of the 3D state and are independent of transition probabilities.

Assuming negligible Russell-Saunders coupling for the collisionally populated nF states for $n \geq 5$, their subsequent radiation via the 3^3D and 3^1D transitions will be in the ratio 3:1. This allows one to calculate contributions to the R.H.S. of Eqs. (39) for singlet and triplet states separately until one reaches the $4F \rightarrow 3D$ contribution. Here one finds the radiation rates must be approximately 1:1 in order to have agreement with $Q'(3^1D)$ and $Q'(3^3D)$ from Table III.

For D states higher than $n = 3$, the F cascade is unable to account for all the excess population of the D states. The discrepancy, denoted by $Q^*(nD)$, must be ascribed to some other populating mechanism. Its magnitude for some of the lower nD states is given in Table VI.

Table VI. Contributions to $Q'(nD)$ in units of 10^{-20}cm^2 .

nD	Cascade		Direct Electron Excitation	Total	$Q'(nD)$ (Table III)	$Q^*(nD)$
	P	F				
3^1D	3.0	40.5	24	67.5	74.5	7
3^3D	2.5	52.0	0	54.5	54.5	0
4^1D	1.0	3.4	13	17.4	42.5	25.1
4^3D	1.0	10.1	0	11.1	24.9	13.8
5^1D	0.3	0.7	7.6	8.6	18.2	9.6
5^3D	0.4	2.2	0	2.6	19.1	16.5
6^1D	0.1	0.2	4.2	4.5	7.0	2.5
6^3D	0.2	0.6	0	0.8	13.0	12.2

If one assumes $Q^*(nD)$ is due to excitation transfer from n^1P , the transfer cross section may be calculated in a manner similar to Eq. (38), i.e.,

$$Q_t(n^1P \rightarrow nD) = \frac{Q^*(nD)}{\bar{v}N} \left[\frac{Q'(n^1P)}{A(n^1P)} - \frac{Q'(nD)}{bA(nD)} \right]^{-1}. \quad (43)$$

Here b is the ratio of the statistical weights of the D state to the P state. These values are presented in Table VII along with values of $Q_t(n^1P \rightarrow nF)$ calculated by Eqs. (37) and (38).

It should be emphasized that these values are not necessarily to be considered as final (except for $n = 3$) but rather to point out difficulties associated with a rigorous application of the multiple state transfer mechanism and other difficulties associated with a return to the original $^1P \rightarrow D$ mechanism.

Discussion of Results

The results obtained here do support the multiple state transfer mechanism to a certain degree. In particular, the transfer $4^1P \rightarrow 4F$ can account for the behavior of $Q'(4F)$ at high pressure both in magnitude and energy dependence. Also, the transfer mechanism $3^1P \rightarrow 3D$ is shown to be unimportant since the excess population of the $3D$ states at high pressure is due to cascade from F states. It also appears that the Russell-Saunders coupling for the $n \geq 5$ nF states is weak and is only appreciable for the $4F$ state, in agreement with the calculations of Lin and Fowler (35). These three conclusions are also in agreement with the experimental work of Kay and Hughes (29)

Table VII. Transfer cross sections from n^1P state in units of 10^{-14} cm^2 .
 ΔE is the approximate energy difference between initial and final states. Error limits on this work are estimated.

n =	3	4	5	6
$\Delta E(n^1P \rightarrow nF) (10^{-3} \text{ eV})$	-	4.9	2.8	1.55
$\Delta E(n^1P \rightarrow nD) (10^{-3} \text{ eV})$	13	5.7	3.0	1.60
$Q_t(n^1P \rightarrow nF)$	-	1.5	2.1	2.3
$Q_t(n^1P \rightarrow nD)$	0.1	.8	1.0	1.0
$Q_t(n^1P \rightarrow n^3D)$	0	.4	1.4	3.3
Total (this work)	.1 ± .1	2.7 ± .3	4.5 ± .5	6.6 ± .7
$Q_t(n^1P \rightarrow nF) \text{ (St. John and Nee)}$	-	1.4	1.9	2.1
$Q_t(n^1P \rightarrow nF) \text{ (Kay and Hughes)}$	-	2.0	6.4	13.

who employed an entirely different experimental technique. These workers measured the effect of collisionally shortened n^1P lifetimes along with F cascade components in the lifetimes of D states. They assumed the only important processes were $^1P \rightarrow F$ transfer and $F \rightarrow D$ cascade. Their transfer cross sections increase with n even more than the total calculated in the present work allowing for $^1P \rightarrow D$ transfer.

St. John and Nee (28) calculated the F state populations at different pressures and electron energies by solving the rather complicated n^1P population equation under the assumption that $Q_t(n^1P \rightarrow nF)$ was proportional to n^x . The predicted D state cascade was compared with observation and gave a good fit to their 3^3D data for $x = 1$ and $Q_t(4^1P \rightarrow 4F) = 1.4 \times 10^{-14} \text{ cm}^2$, or $x = 2$ and $Q_t(4^1P \rightarrow 4F) = 1.2 \times 10^{-14} \text{ cm}^2$. However, they also found that on the $n = 4$ level the predicted F cascade was not quite sufficient for all 4^3D excess population and even less sufficient for the 4^1D state. The model $x = 1$ of St. John and Nee was used for comparison in Table VII. There is good agreement in the $n^1P \rightarrow nF$ cross sections with this work.

It appears therefore that the simple model of $^1P \rightarrow F$ transfer and $F \rightarrow D$ cascade is not sufficient to account for all the observations described in this chapter. For the F state cascade to be equal to the observed excess of $Q'(nD)$, for low n , would require $Q'(nF)$ to increase with n . This can be seen from consideration of the matrix equation for the cascade process

$$(B^{-1})Q'(F) = Q'(D) - Q_{ec}(D) \quad (44)$$

where (B^{-1}) is the triangular infinite matrix whose most important elements are given in Table V, $Q'(F)$ is a vector whose n th component is $Q'(nF)$, and the R.H.S. is a vector whose components are $Q'(kD)$ corrected for direct electron excitation and P cascade by $Q_{ec}(kD)$. Assuming that the inverse branching ratios $B^{-1}(nF \rightarrow kD)$ approach a limit with high n as is indicated in Table V, and neglecting the small P cascade term to $Q'(kD)$, one may calculate the $Q'(nF)$ needed to satisfy $Q'(kD) - Q(k^1D)$. The results are given in Table VIII.

These difficulties can be removed on the $n = 4$ level by allowing the possibility of a transfer interaction $4F \rightleftharpoons 4D$. Even though $\Delta L = 1$, $\Delta E = 0.0008$ eV, so such a reaction should be favored over $n^1P \rightarrow nD$, where $\Delta L = 1$ and $\Delta E = .0057$ eV. Since the $4F$ has both singlet and triplet character, the $4F \rightarrow 4^3D$ transfer would remove the violation of the spin rule inherent in the assumed $^1P \rightarrow ^3D$ interaction. Calculations show that a transfer cross section $Q_t(4^3F \rightarrow 4^3D) \approx 1.7 \times 10^{-14} \text{ cm}^2$ would account for $Q^*(4^3D)$.

For the $n \geq 5$ levels, the situation becomes even more complicated. One suspects some depopulating mechanism is at work on the nF states due to the rapid decrease of $Q'(nF)$ with n and the subsequent slow increase of $Q_t(n^1P \rightarrow nF)$ with n . Transfer processes such as $5G \rightleftharpoons 5^3D$, $6F \rightleftharpoons 6H$, with $\Delta L = 2$ and small ΔE , may be needed to completely remove violation of the spin rule and account for the small $Q'(nF)$ for the higher n states.

At first glance, electron-ion recombination processes might seem to account for the observed behavior of the D states. The energy dependence of $Q'(nD)$ at high pressure, while similar to the n^1P states,

Table VIII. Distribution of F state apparent cross sections needed to satisfy branching ratios and observed Q' (kD) excess.

k,n	Q' (kD)-Q(k ¹ D) (10 ⁻²⁰ cm ²)	Q' (nF) (10 ⁻²⁰ cm ²)
3	105.	-
4	54.4	16
5	29.6	15
6	15.8	25
7	8.3	29
8	3.8	37
9	1.9	23
10		20
>10		58

is also similar in shape to the ionization cross section curve for helium. Since the energy distribution of the ionized off electrons is sharply peaked at very low energy (36), and since neglecting these give a positive potential of several volts in the electron beam (37), one might argue the possibility that sufficient trapping of the slow electrons occurs to allow significant recombination. Granting this, one might further point out that since the calculated recombination coefficients favor high angular momentum (38), and favor triplet states over singlets (39), then observed effects might be attributed to such a process.

Using the hydrogenic recombination coefficients α calculated in Ref. 38 for 300 °K, one can calculate the electron density n_e needed to support the radiative dropout of, say, the 5^3D state expressed by $Q^*(5^3D)$ in Table VI.

Thus

$$\alpha(5^3D)n_e^2 = Q^*(5^3D) \frac{IN}{eS} \quad (45)$$

and for 63 μ pressure, 1×10^{-3} amp beam current, $n_e = .8 \times 10^{13} \text{ cm}^{-3}$. Such an electron density is considerable and this rate could only be sustained if almost all slow electrons produced underwent volume recombination. This is easily seen from equating production rate per cm^3 to recombination rate per cm^3 .

Thus

$$Q_i \frac{IN}{eS} = \alpha_T n_e^2 \quad (46)$$

where Q_i is the ionization cross section and α_T the total recombination

coefficient. Eq. (46) gives $n_e = 1.1 \times 10^{13} \text{cm}^{-3}$. However, $\alpha(3^3D) = 2.6 \alpha(5^3D)$ implying $Q^*(3^3D) = 43 \times 10^{-20} \text{cm}^2$ which would necessitate small F cascade to 3^3D , contrary to observation. Although Eq. (46) would give a linear dependence of $Q^*(n^3D)$ with beam current, it is difficult to visualize total volume recombination at all pressures, and certainly wall recombination must become important at some pressure. This would show up as a non-linearity of $Q^*(n^3D)$ with I at some pressure, contrary to observation.

One sees from Figs. 17 and 18 that the 1P and D states for high n show increasing depopulation effects as the pressure is increased. Since the small values of $Q'(nF)$ at high n and 63μ indicate these states do not receive a large populating effect at high pressure, one is faced with the question of what states are populated at the expense of these states. If one picked a level, say $n = 10$, and followed the excitation transfer process from state to state of increasing angular momentum, remembering that $\Delta n = 0$, one would expect a populating effect with pressure at least by the time one reached $L = 9, n = 10$. Since radiative transitions favor decreasing L and low n, such a transfer of excitation would eventually tend to preferentially populate low n low L states with increasing pressure as observed. On the basis of such a cyclic process, one would expect the $5G \rightarrow 4F$ radiation at approximately 4 microns wavelength to be considerable.

The possibility of considerable $G \rightarrow 4F$ cascade raises some interesting questions concerning the observed pressure dependence

of the 4F apparent cross section as given in Fig. 20. If one supposes that the only populating process of the 4F state is due to transfer from the 4¹P state, then for pressures below about 30 μ one must have $Q'(4F) \propto N^2$. This is because $Q'(4^1P) \propto N$. As has been shown, one may fit the data with an "s" shaped curve with a slope of one in its central portion by assuming $Q_{ec}(4F) = 1.3 \times 10^{-19} \text{ cm}^2$. Theoretical calculations of a highly sophisticated nature (Chun C. Lin, private communication) indicate a value of only $0.54 \times 10^{-20} \text{ cm}^2$ for the direct electron excitation part of $Q_{ec}(4F)$. The data points of the 4F state in Fig. 20 show enough scatter at low pressure to allow a linear decrease of the apparent cross section with pressure which could eventually approach the calculated value at a very low pressure of 0.4 μ . Such a small direct electron excitation cross section would imply that $Q_{ec}(4F)$ is mostly due to either G state cascade or some unknown populating process.

There is too much consistency in the data to allow for significant error in the measured value of $Q'(4F)$. Such error would significantly affect the fact that the total measured input into the 3D levels is within 5 per cent of the measured output from these levels at 63 μ . Indeed, even at 8 μ pressure, the 4F apparent cross section alone (about $15 \times 10^{-20} \text{ cm}^2$) accounts for much of the pressure dependent 3D apparent cross section ($18 \times 10^{-20} \text{ cm}^2$).

The radiation 4¹D \rightarrow 3¹P at 19,094 \AA and 63 μ is well resolved. The various theoretical calculations of the branching ratio for this radiation are in good agreement. This might be expected in view of

the fact that the 4^1D state may only radiate to two lower states, whereas a state like the 6^3D (mentioned earlier) may radiate to 6 lower levels and consequently show poorer agreement among various theoretical calculations. Since the $4^1D \rightarrow 3^1P$ and $4F \rightarrow 3D$ transitions are only separated by a small wavelength interval, the standardization parameters may be assumed to be equal for each. The apparent cross section for the $4F$ state should then be equal to the product of 3 quantities, i.e., the ratio of the intensities of the 18,695 and 19,094 Å radiation, the branching ratio for the $4^1D \rightarrow 3^1P$ radiation, and the apparent cross section of the 4^1D state (presented in Table III). This gives $5.75 \times 0.27 \times 42.5 \times 10^{-20} = 66 \times 10^{-20} \text{ cm}^2$ as compared to the independently measured value of $69 \times 10^{-20} \text{ cm}^2$.

CHAPTER VI

THE TEMPERATURE DEPENDENCE OF EXCITATION TRANSFER

Description of Experiment

Purpose

The work described in this chapter was actually undertaken prior to that described in the earlier chapters. At the time this work was undertaken, the multiple state transfer mechanism was thought sufficient to rigorously account for all excess 3D populations at high pressure. Some anomalies in data interpretation resulted which can now be accounted for in the light of the discussions of Chapter V.

The basic idea of this experiment was to obtain information concerning the dependence of the transfer process on the relative velocity of the colliding systems. This was to be accomplished by measuring the temperature dependence of the various experimental parameters associated with the population equations of the interested states. This necessitated the following specialized equipment.

The Vacuum Furnace

A diagram of the vacuum furnace is shown in Fig. 22. Heating in the central zone is produced by radiation from hot tungsten filaments.

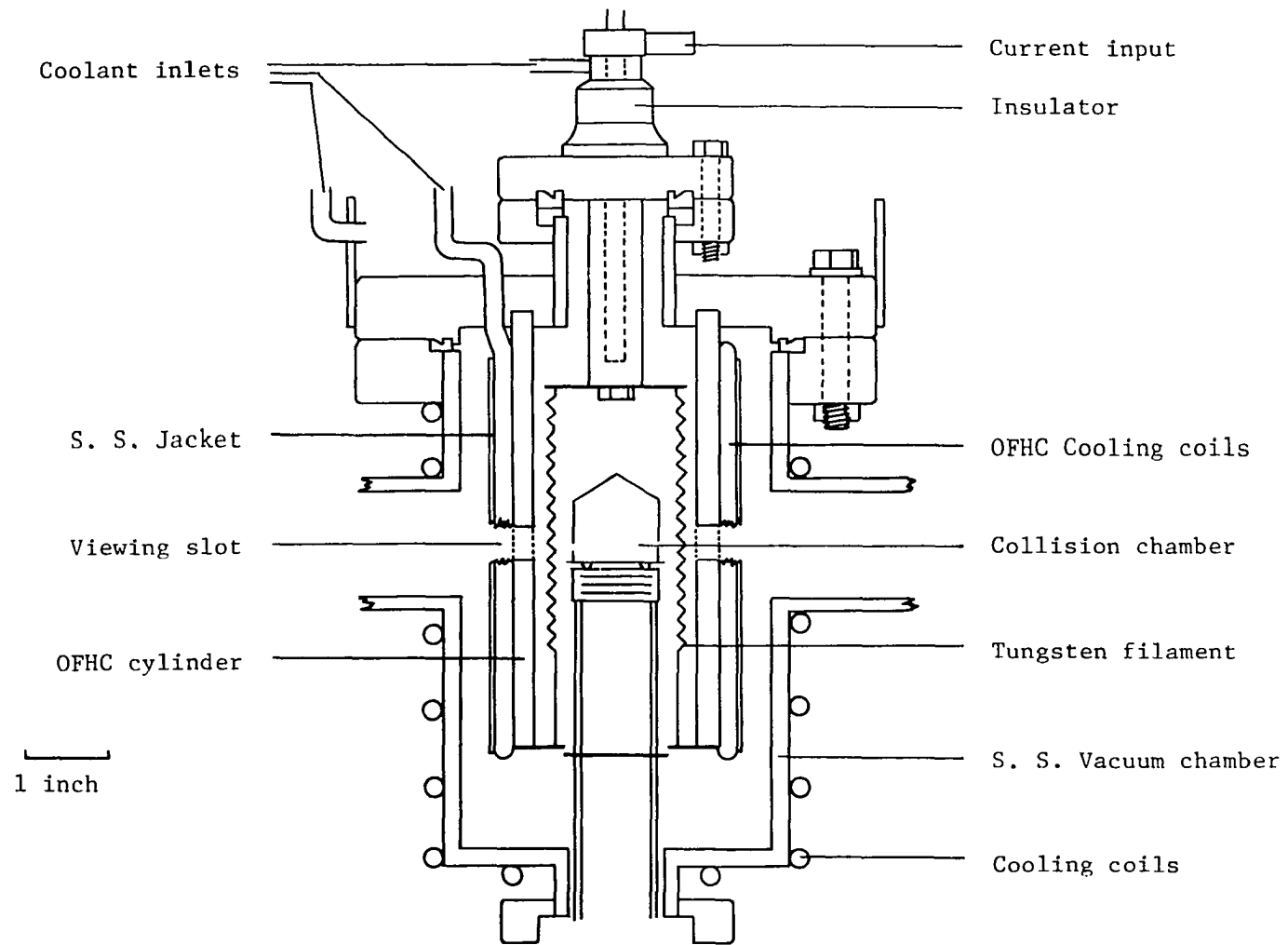


Figure 22. The vacuum furnace

There are 30 filaments, each 11 cm in length and arranged with cylindrical symmetry. Each filament is helically wound (28 turns) of 0.015 inch diam. wire. The windings are alternately clockwise and counter clockwise to provide for magnetic field cancellation. About 9 amperes of current per filament produced a filament temperature of approximately 2500 °K. Surrounding the filament assembly is an OFHC* copper cylinder which is maintained at near room temperature by coolant coils. These are also of OFHC copper and their total length inside the vacuum chamber is about 6 feet. The cylinder had 12 longitudinal slots milled into its outside surface to accommodate the cooling coils. These were pressed into the slots and clamped with a stainless steel retaining jacket. The copper cylinder is highly polished and serves as a reflector to concentrate the radiant energy from the filaments toward the axis of the cylinder. The OFHC current input at the top of the chamber was drilled to accommodate coolant flow. The outside and bottom of the chamber are jacketed with coolant coils and the top of the chamber serves as the base of a circulated open top water reservoir. The filament support discs are constructed of 0.020" molybdenum.

The power source is a 3-phase rectifier rated at 500 amperes at 6 V. An A.C. source would tend to produce large fluctuating electromagnetic fields inside the furnace.

* Oxygen-free, high conductivity.

The High Temperature Electron Gun

The electron gun, shown in Fig. 23, was actually designed to operate at much higher temperatures than it was subjected to in this experiment. Refractory materials used were tantalum, tungsten, molybdenum, and sapphire. It is difficult to assemble such materials by spot welding techniques. Even when accomplished, bimetallic welds may cause flexure with temperature changes. Nuts and bolts of these materials are not available in the required sizes nor can they be readily machined. For these reasons, the electrical leads to the various electrodes are under spring tension. This maintains the entire gun structure in a rigid configuration while allowing easy dismantling for maintenance.

The electron gun is essentially a tetrode device employing shaped focusing electrodes (40) and an oxide coated cathode. The beam was collimated to 1 mm diam. before entering the Faraday cage. Energy resolution was determined by the retarding potential difference method to be about 0.8 eV at 100 eV energy. In this method, the Faraday cage potential is made to approach that used to accelerate the electrons. The current cut-off curve may be differentiated to yield the energy distribution curve. See Fig. 24.

The entire gun assembly is inserted into the central region of the furnace where it is heated by radiation absorption from the tungsten filaments. The interior of the Faraday cage is fitted with 8 radial fins extending from the wall toward the beam. This increases the interior surface area and allows for better gas-surface

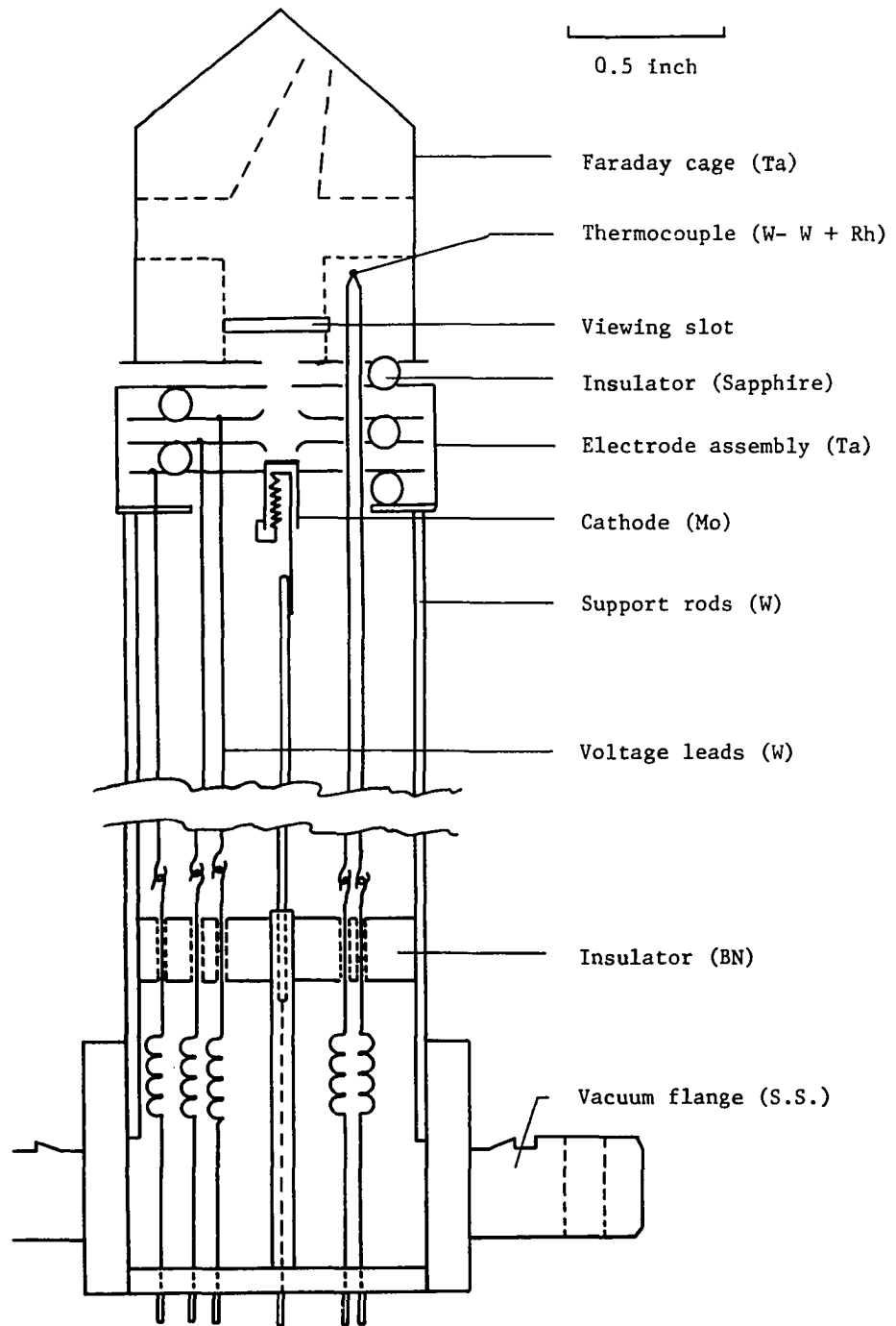


Figure 23. The high temperature electron gun.

RETARDING POTENTIAL (Volts)

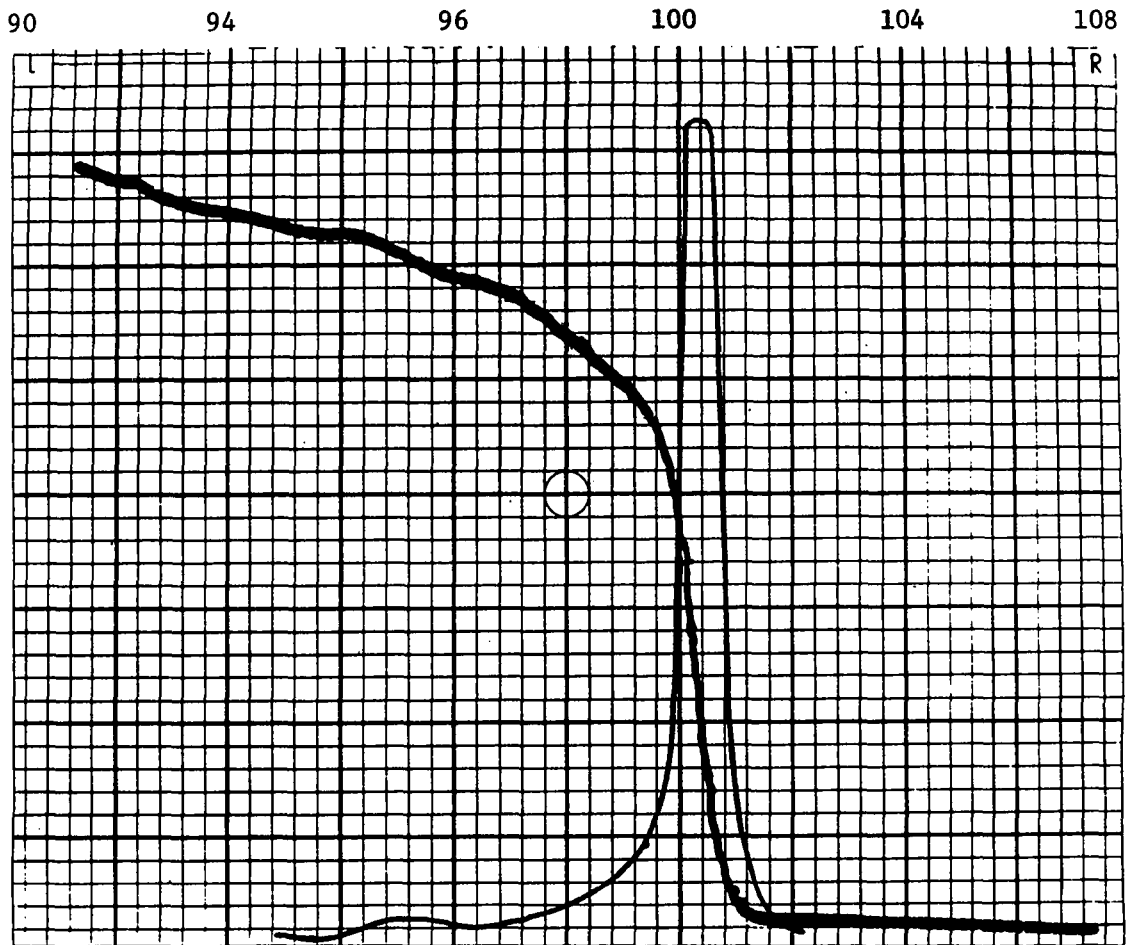


Figure 24. Oscillogram of beam current versus retarding potential. The negative differential (drawn in) indicates a half peak energy spread of 0.8 volts.

temperature equilibrium. A tungsten-tungsten + 26% rhenium thermocouple is attached to one fin and serves as an indication of the interior surface temperature. The thermocouple also serves as beam current to ground return. The thermocouple voltages were measured to within $\pm 5 \times 10^{-6}$ V. A calibration curve of temperature versus voltage as given in Ref. 41 was used. This was corrected to proper cold junction temperature. This curve was checked by comparing thermocouple temperatures against a calibrated mercury thermometer in a circulated oil bath up to 700 °K. The interior Faraday cage temperature versus furnace current is shown in Fig. 25.

The excitation radiation was observed through a slot in the Faraday cage. This slot is lined up with a similar one on the opposite side of the Faraday cage, and these in turn are aligned with slots in the corresponding sides of the reflector. The rear window of the vacuum chamber was replaced with a light trap. A dark background is thus provided for observation of the beam excitation.

Cathetometer measurements indicated that the vertical shift of the electron gun due to thermal expansion of the supporting structure was not more than 0.003". The beam homogeneity in a vertical direction is such that a small displacement on this order is undetectable.

The effect of the rectifier ripple current on the electron beam was also found to be undetectable. This was checked by tuning the detection equipment to the frequency of the ripple.

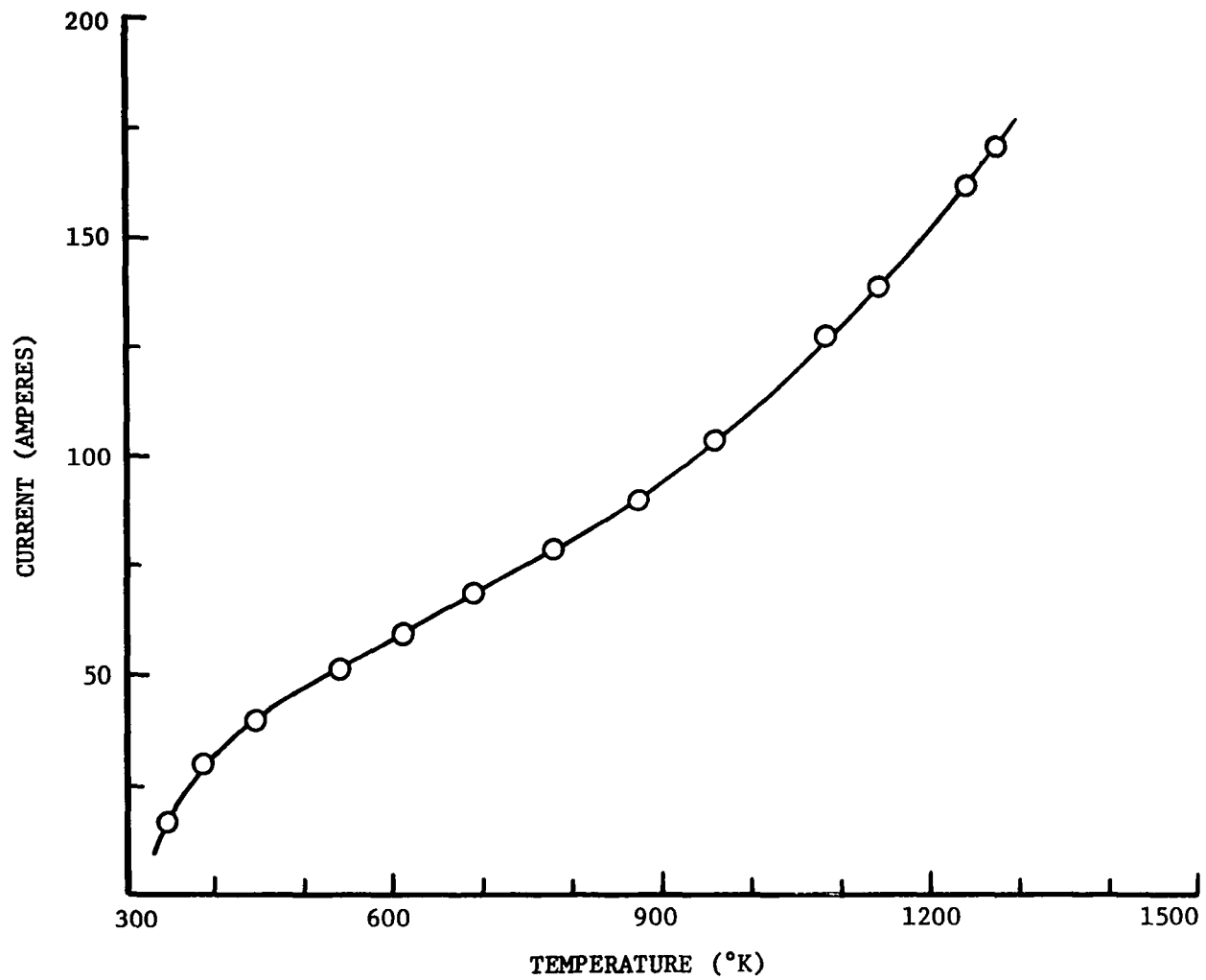


Figure 25. Faraday cage temperature versus furnace current.

Data Acquisition

The light detection equipment used was essentially the same as that shown in Fig. 2. In spite of the slot arrangement in the Faraday cage, some background radiation entered the optical system from the furnace region at the higher Faraday cage temperatures. The excitation radiation was modulated at 100 cps and had a usable signal to noise ratio provided its intensity was greater than about 0.3 per cent of the blackbody background radiation. For the 5876 Å radiation, this limit was reached at a Faraday cage temperature of about 1000 °K. Much background radiation at this temperature was due to reflection from the 1600 °K tungsten heating filaments. A "dummy" beam consisting of a neon glow tube was placed so as to be visible through the Faraday cage slots. This was modulated at 100 cps and A. C. detected while the Faraday cage was heated to 1000 °K. The 5764 line intensity remained constant up to 800 °K and increased by 2 per cent from 800 °K to 1000 °K. No useful data could be obtained for spectral lines in the red or infrared.

The variation of $Q'(k)$ with temperature was determined by measuring the variation of $I_p(k \rightarrow j)/IN$ with temperature. The main difficulty here was to obtain the ground state density inside the Faraday cage as a function of temperature. The procedure finally adopted was as follows:

The intensity of the radiation $5^1S \rightarrow 2^1P$ at 40 eV impact energy shows good linearity with pressure since it is affected only by

direct electron excitation and only 2 per cent P cascade. I_p/I for this radiation versus pressure is shown in Fig. 26. If one knows the ground state density inside the Faraday cage at 300 °K from pressure measurements in the system outside the cage (also at 300 °K), then one may use I_p/I for the 4438 Å radiation to determine the ground state density for higher temperatures. N versus temperature is given for several temperatures in Fig. 27. One may also calculate the density of a gas at temperature T inside a nearly closed can by consideration of the flux through an opening small compared to the mean free path. If the gas outside the can is at temperature T_0 then

$$\frac{1}{4}N(T_0) \bar{v}(T_0) = \frac{1}{4}N(T) \bar{v}(T) \quad (47)$$

giving

$$N(T) = N(T_0) \left(\frac{T_0}{T} \right)^{\frac{1}{2}} \quad (48)$$

Due to the large surface area of the cooled reflector seen by the gas outside the Faraday cage, one would expect it to have a velocity distribution and density characteristic of 300 °K. The density $N(T)$ calculated from Eq. (48) with $T_0 = 300$ °K is also shown in Fig. 27 and shows reasonable agreement with the $N(T)$ deduced from the 4438 Å radiation.

Although apparent cross sections versus temperature were obtained for several other states, only those of the 4^1P , 3^3D , and 4^3D states are amendable to some degree of unambiguous interpretation at the present time. The gas in the system exterior to the

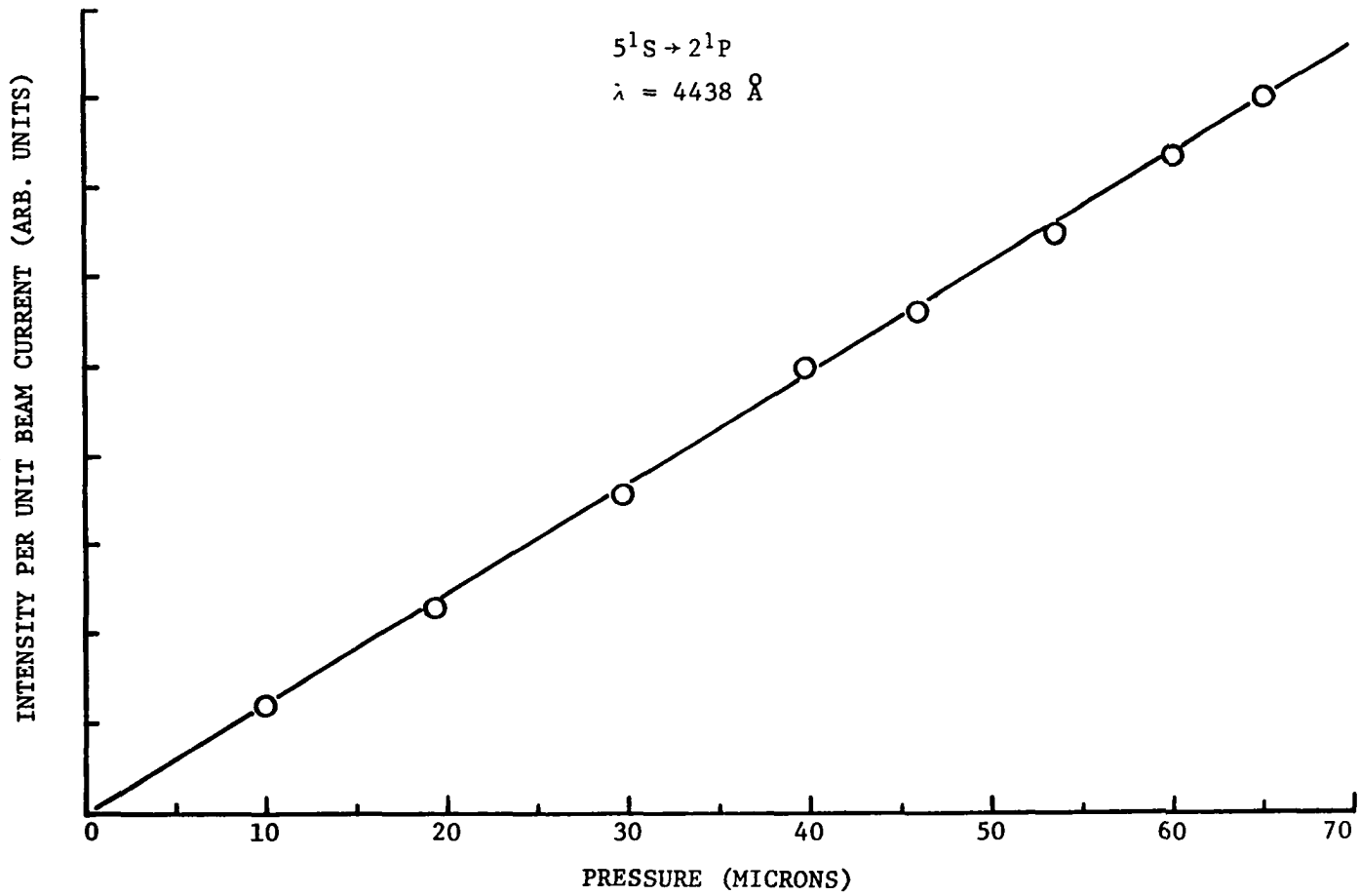


Figure 26. Intensity per unit beam current versus pressure for the 5¹S → 2¹P transition.

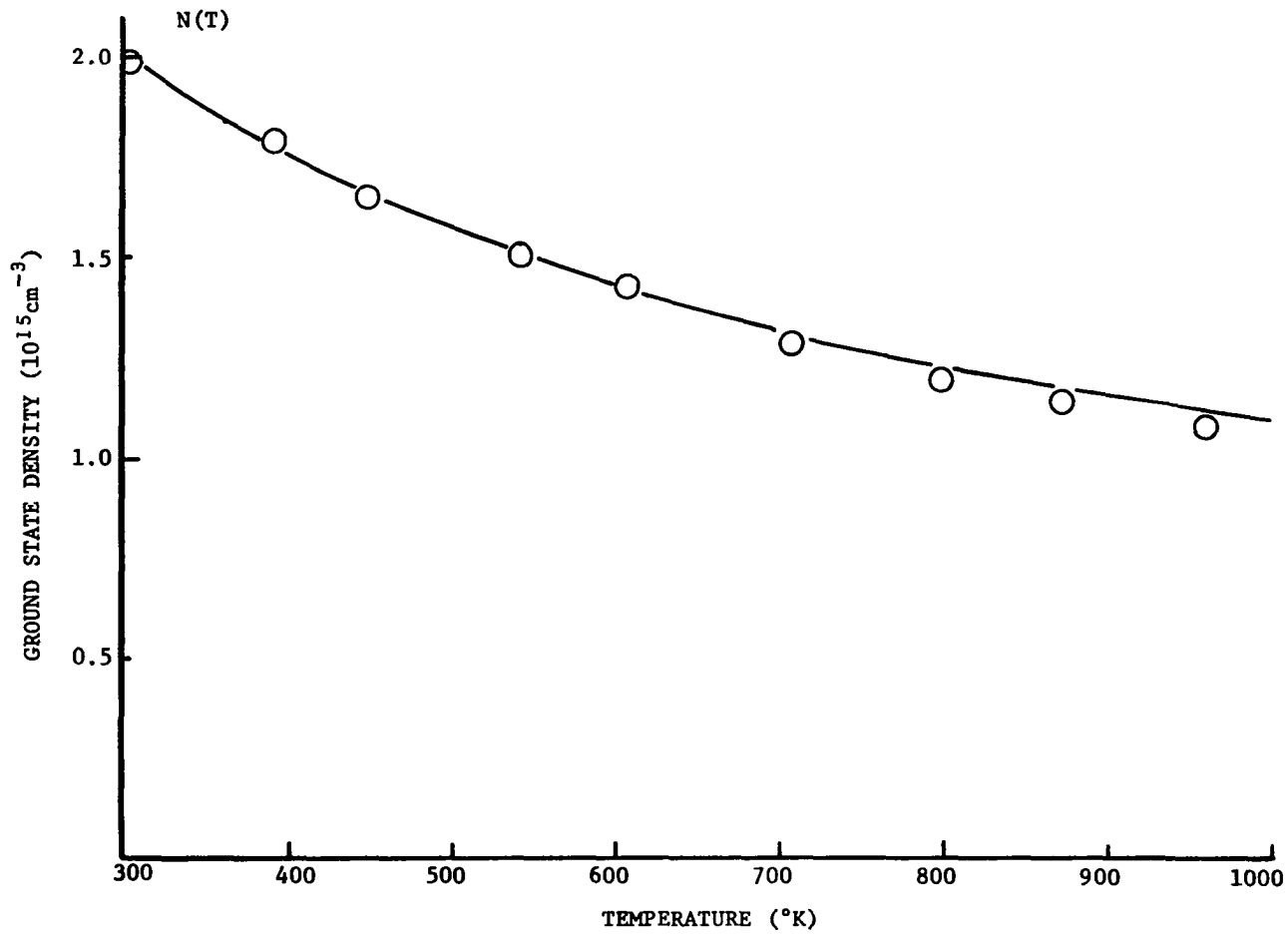


Figure 27. The ground state density $N(T)$ versus temperature. The data points are from the 4438 \AA radiation. Solid line is from Eq. (48).

Faraday cage was continuously monitored at 63μ pressure by a Pirani gauge and the excitation energy held at 100 eV. The $Q'(k)$ versus temperature curves were normalized to their values at 300 °K. In a previous calculation (42), the values of the apparent cross sections at 300 °K were obtained by comparison with the 3^3D value given in Ref. (28). This gave 52, 26.6, and $2550 \times 10^{-20} \text{ cm}^2$ for the 3^3D , 4^3D , and 4^1P values respectively. For the present calculation we will use the values 54.5, 24.9, 2600×10^{-20} which were determined in the more recent measurements of Table III. $Q'(k)$ vs. T are shown in Figs. 28, 29, and 30.

Analysis of Data

On the basis of the multiple state transfer theory, and neglecting the small P cascade and electron excitation gain, one may write the following equations:

$$Q'(3^3D) = c \sum_{n=5}^{\infty} B^{-1}(nF \rightarrow 3D)Q'(nF) + d Q'(4F) \quad (49)$$

$$Q'(4^3D) = c \sum_{n=5}^{\infty} B^{-1}(nF \rightarrow 4D)Q'(nF) \quad (50)$$

Here, c is the fraction of nF atoms, $n > 4$, that are triplet in nature and d is the fraction of $4F$ atoms that are triplet in nature. From Table V one sees that to a good approximation $B^{-1}(nF \rightarrow 3D) \approx a_4 B^{-1}(nF \rightarrow 4D)$ up to $n = 12$ where $a_4 \approx 1.66$. Using this relation in Eq. (50) and subtracting Eq. (50) from Eq. (49) gives

$$Q'(4F) = \frac{1}{d} [Q'(3^3D) - a_4 Q'(4^3D)] \quad (51)$$

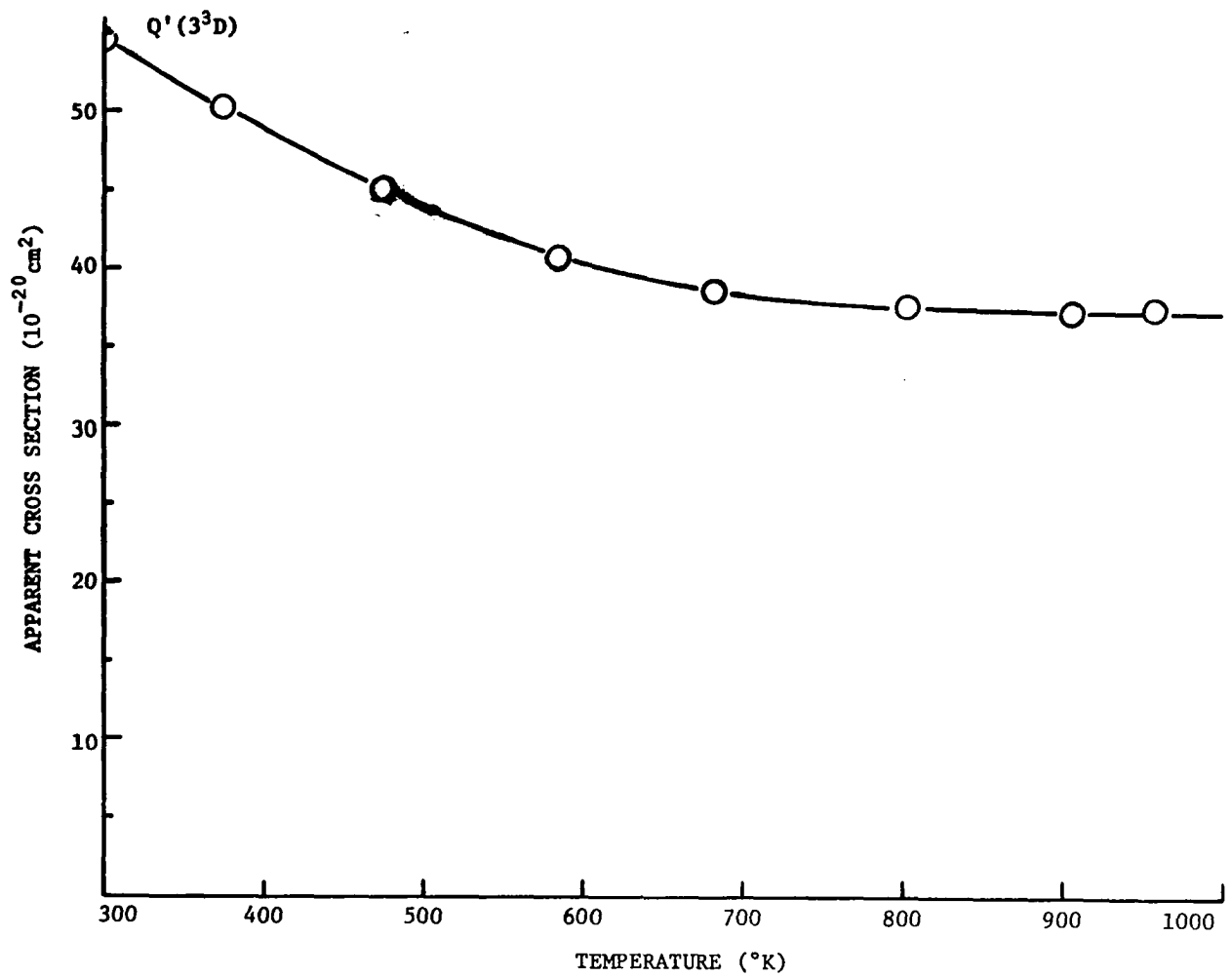


Figure 28. The apparent cross section of the 3^3D state versus temperature.

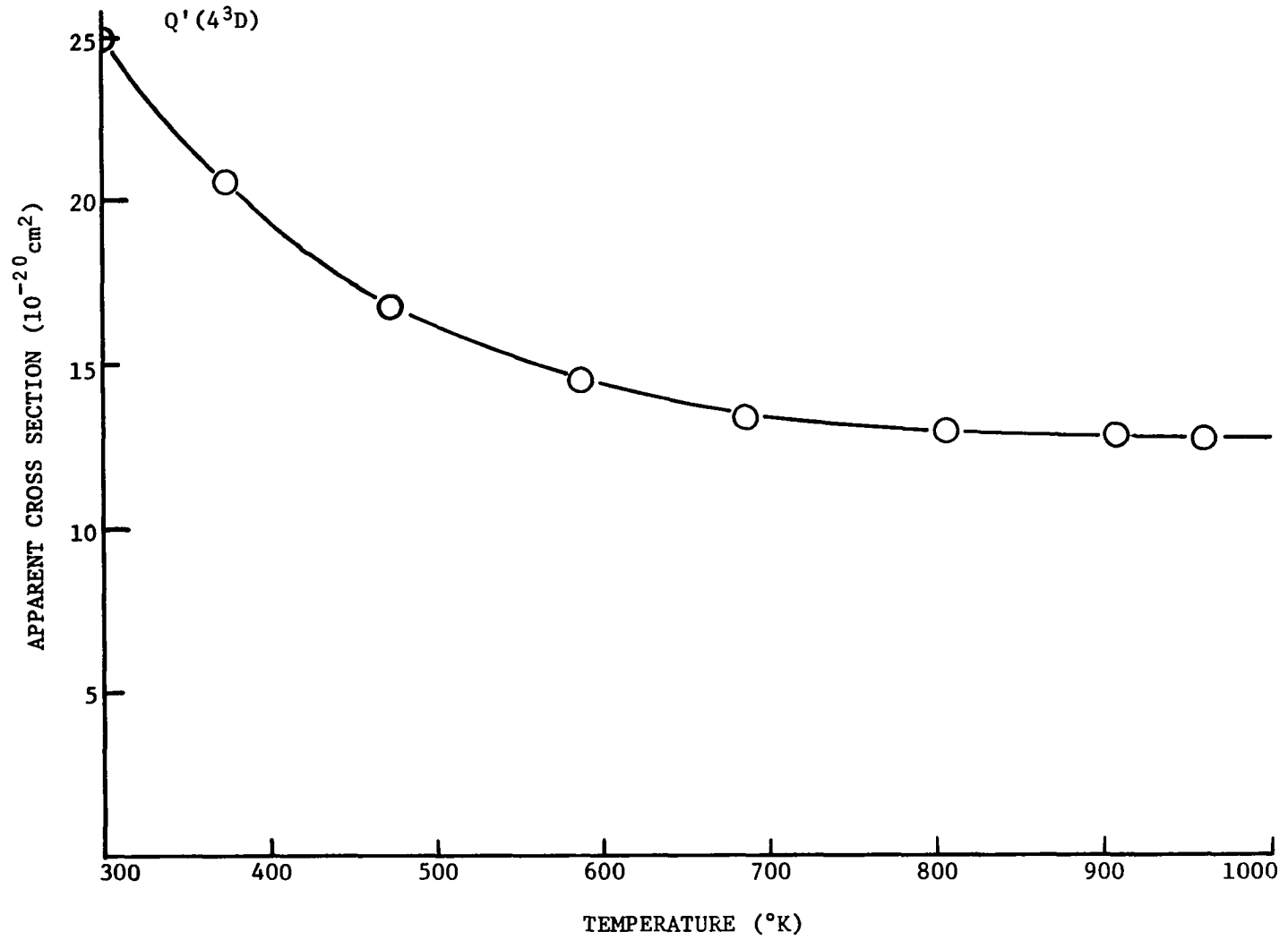


Figure 29. The apparent cross section of the 4^3D state versus temperature.

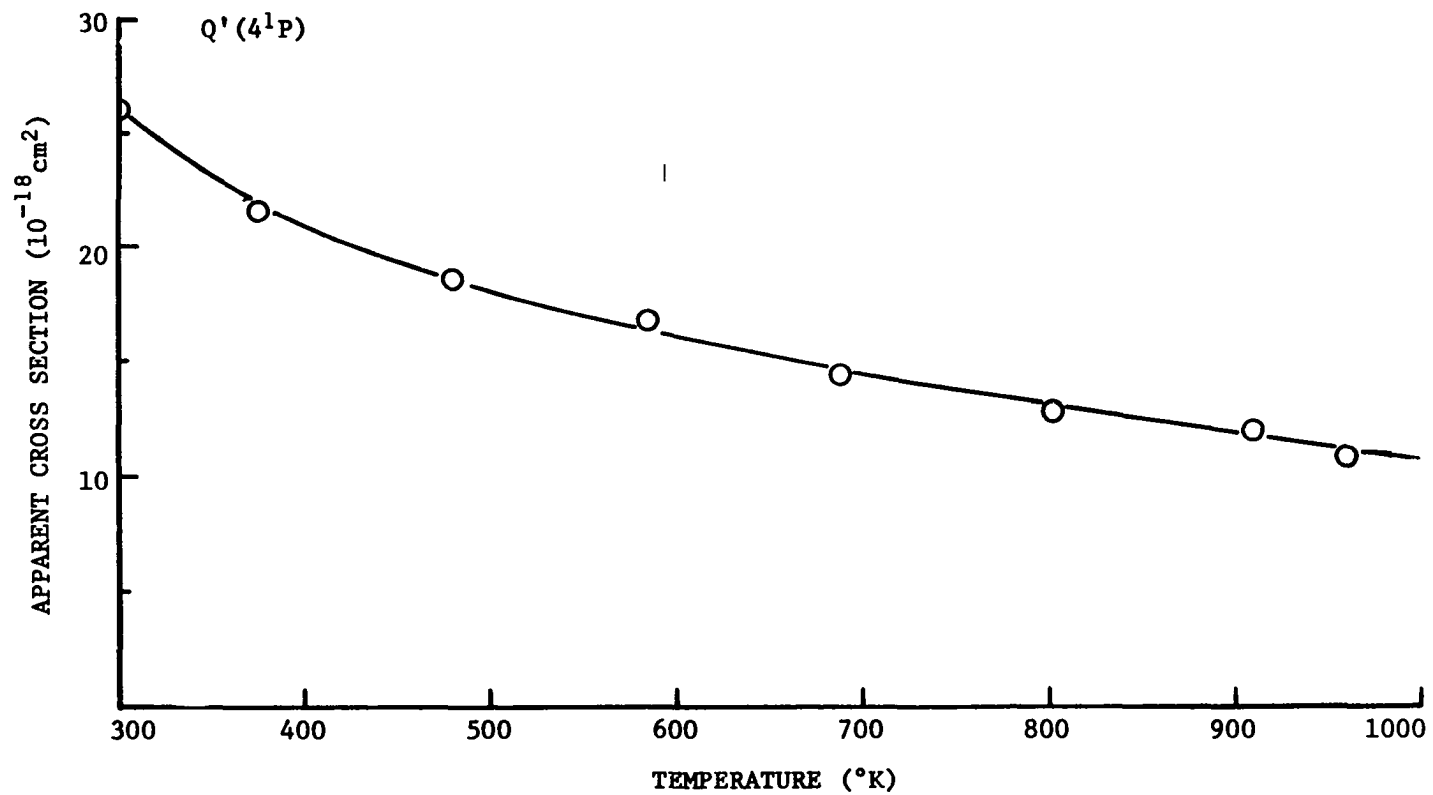


Figure 30. The apparent cross section of the 4^1P state versus temperature.

Using Eq. (38), Chapter V, one obtains

$$Q_t(4^1P \rightarrow 4F) = \frac{\frac{1}{d} [Q'(3^3D) - a_4 Q'(4^3D)]}{\bar{v}N \left[\frac{Q'(4^1P)}{A(4^1P)} - \frac{1}{d} \frac{1}{bA(4F)} [Q'(3^3D) - a_4 Q'(4^3D)] \right]} \quad (52)$$

The data in Chapter V indicated a value of $d = \frac{1}{2}$, and consequently $b = 14/3$. The quantity \bar{v} may be calculated from the distribution function in Ref. (43) as

$$\bar{v} = 4(kT/\pi m)^{\frac{1}{2}} . \quad (53)$$

This equation assumes a Maxwellian velocity distribution of the gas in the Faraday cage characteristic of the wall temperature T . The accommodation coefficient of helium on tantalum is approximately 0.04 from Ref. (44). This means that on the average an atom with energy corresponding to 300 °K will need 25 wall collisions before it acquires an energy characteristic of the wall temperature. By coating the inside of the Faraday cage with graphite, the accommodation coefficient is increased so that only about 10 wall collisions are required. The solid angle subtended at the center of the Faraday cage by the apertures in the wall is about $0.014 \times 4\pi$. Since the mean free path is on the order of the radius, the probability that an atom having a random direction will undergo a wall collision is roughly $(1 - 0.014)$, and for 10 such collisions this probability is

$(1-.014)^{10}$ or about 0.9. The probability of a wall collision is increased by increasing its surface area through the radial fin arrangement mentioned earlier. Other verification that the distribution in the can is approximately Maxwellian is that the density in the can followed from the flux formula.

As one sees from Fig. 30, the apparent cross section of the 4^1P state drops with increasing temperature. Since one may calculate the depopulating effect due to Doppler broadening of the resonance line, any remaining temperature dependence may be ascribed to transfer depopulation. The population equation for the 4^1P state may be written

$$Q_{ec}(4^1P) \frac{IN}{eS} + (1-g)N(4^1P)A(4^1P \rightarrow 1^1S) + \bar{v}NN(4F) \frac{1}{b} Q_t(4^1P \rightarrow 4F) = \bar{v}NN(4^1P)Q_t(4^1P \rightarrow 4F) + N(4^1P)A(4^1P) . \quad (54)$$

Using the definition of apparent cross section, one finds after some algebraic manipulation

$$Q_t(4^1P \rightarrow 4F) = \frac{Q_{ec}(4^1P) - Q'(4^1P)[gA(4^1P \rightarrow 1^1S) + A(4^1P \rightarrow j)]/A(4^1P)}{\bar{v}N \left[\frac{Q'(4^1P)}{A(4^1P)} - \frac{Q'(4F)}{b A(4F)} \right]} \quad (55)$$

Here $A(4^1P \rightarrow j)$ denotes transition probability to all states other than 1^1S . The only quantity here which is an unknown function of temperature is $Q'(4F)$. At 300 °K the second term in the denominator is only

10 per cent of the first and could be neglected for a zeroth order approximation. A better approximation would be to retain this term and consider it constant at its room temperature value. Taking $Q_{ec}(4^1P) = 158 \times 10^{-20} \text{ cm}^2$ from Ref. (5), and $Q_t(4^1P \rightarrow 4F)$ from Table VII, Eq. (55) may be solved for g at room temperature in terms of known quantities. The quantity g is a function of the absorption coefficient k and imprisonment radius ρ . From the graph in Ref. (1) one has

$$g(k\rho) \approx 0.9(k\rho)^{-1.2}, \quad k\rho > 6. \quad (56)$$

The temperature dependence of the absorption coefficient is seen from the relation

$$k(T) = \frac{\lambda^3 w(4^1P)}{8\pi^{3/2} w(1^1S)} A(4^1P \rightarrow 1^1S) \left(\frac{m}{2kT} \right)^{1/2} N(T). \quad (57)$$

Here $\lambda = 3965 \text{ \AA}$ and the w 's are statistical weights. At $300 \text{ }^\circ\text{K}$, $\rho = 63\mu$, $k = 40 \text{ cm}^{-1}$ giving $\rho = 1.3 \text{ cm}$ from Eq. (56). Since $N(T)$ is known, $k(T)$ may be calculated at higher temperatures yielding values of g through Eq. (56).

Discussion of Results

The temperature dependence of the transfer cross sections is obtained by substitution of measured and calculated quantities in the right-hand side of Eq. (52) or Eq. (55). The results for

the two methods of calculating $Q_t(4^1P \rightarrow 4F)$ are given in Fig. 31. One notices that the value of $Q_t(4^1P \rightarrow 4F)$ calculated from Eq. (52) at 300 °K is only about one-half the value which was calculated from $Q'(4F)$ in Chapter V. This discrepancy is due to the assumption in Eq. (50) that all the 4^3D is due to F cascade. Adding the term $Q^*(4^3D)$ from Table VI to the right-hand side of Eq. (50) would give the same $Q_t(4^1P \rightarrow 4F)$ as deduced in Chapter V. In view of the unknown nature of the source and temperature dependence of the additional populating term $Q^*(4^3D)$, a quantitative interpretation of $Q_t(4^1P \rightarrow 4F)$ as given in Fig. 31 would be difficult.

If one attempted to pursue this method of analysis to higher states, some difficulty is encountered, Calculation of Eq. (51) for higher states would yield

$$Q'(nF) = \frac{1}{c} [Q'(n-1 \ ^3D) - a_n Q'(n^3D)] \quad . \quad (58)$$

The requirement that $Q'(nF)$ be positive sets a limit on the relative sizes of the apparent cross sections of any two neighboring 3D states. This is not realized to within experimental error on the $n = 4, 5$, and 6 states as can be seen from the "crowing" together of these states at high pressure in Fig. 17. The transfer "hump" at 100 eV on the 5 and 6 3D excitation functions is also more pronounced than on the other 3D functions.

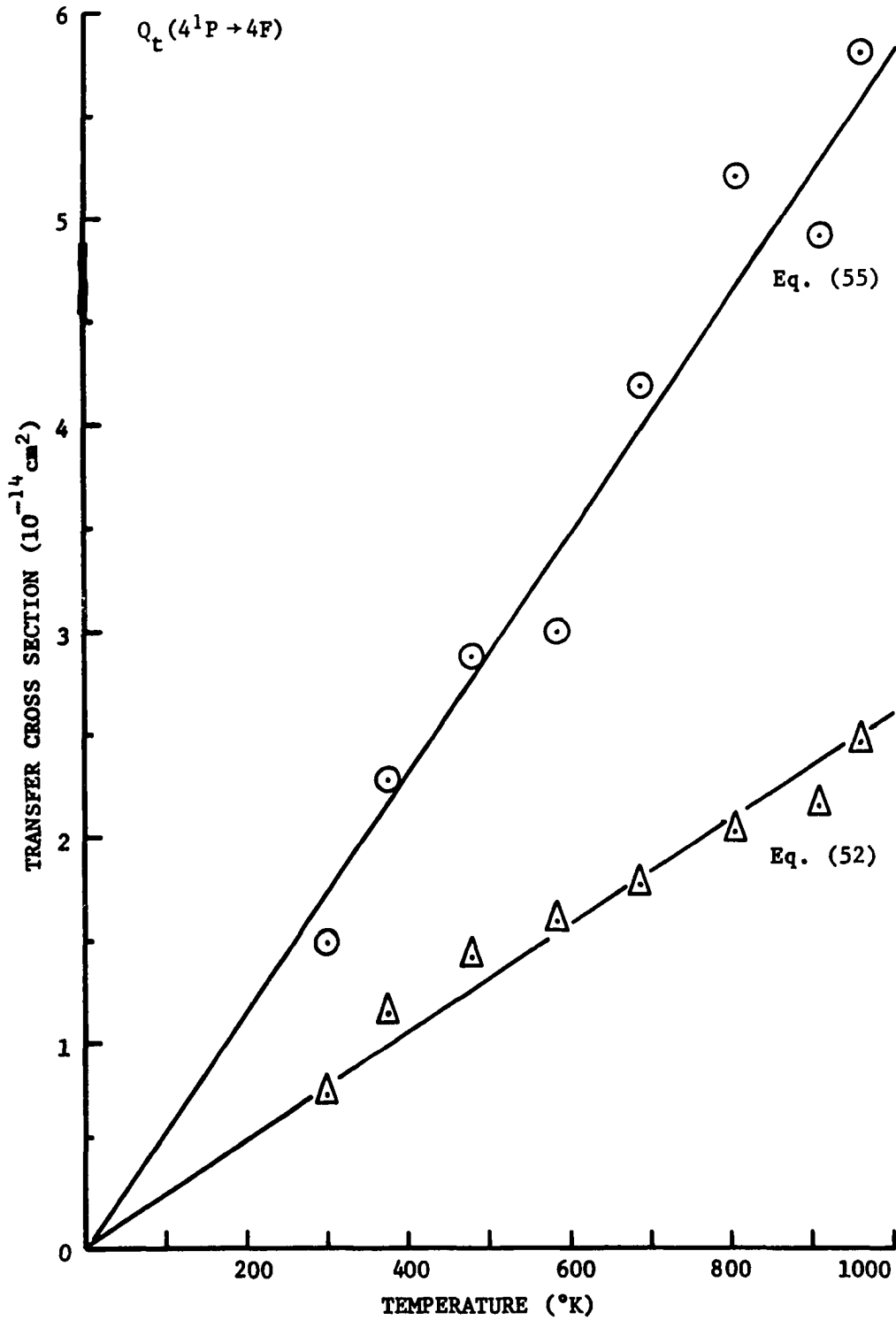


Figure 31. The 4^1P to $4F$ transfer cross section versus temperature.

The transfer cross section calculated from Eq. (55) should be considered as more reliable. The calculated points shown in Fig. 31 show considerable scatter but seem to show a linear dependence with temperature. If one were to assign error bars to these points on the somewhat arbitrary basis of ± 5 per cent deviation in the apparent cross sections used, one would indeed find a linear relation with temperature to within experimental error. This also applies to the data calculated from Eq. (52). It was pointed out in the preceding paragraph that consideration of the term $Q^*(4^3D)$ would cause agreement in the values of $Q_t(4^1P \rightarrow 4F)$ at room temperature. Allowing this term to be due to a populating process that increased linearly with temperature would produce reasonable agreement at the higher temperatures also.

One particular motivation for this experiment was to test the hypothesis presented in Ref. (26) that very high n states, say $n = 15$ to $n = 24$, were responsible for the observed pressure effects of the low nD levels. Here it was argued that states higher than about $n = 24$ would be collisionally ionized at room temperature since $E(\infty) - E(n)$ is less than kT . Hence such states would not contribute to the transfer process. At 1000 °K, the energy of relative motion is sufficient to ionize states higher than about $n = 12$. However, the values of $Q'(3^3D)$ and $Q'(4^3D)$ at this temperature are little different from what one would expect from pressure effects alone. It

is therefore concluded that states higher than $n = 12$ have little effect on the 3^3D and 4^3D populations. This is again in agreement with the results of the preceding chapter.

CHAPTER VII

Conclusion

Helium gas has been bombarded by electrons under controlled conditions of pressure, temperature, electron energy and beam current. Radiation rates from 51 transitions have been measured over the spectral range of 3230 to 20,582 Å.

The apparent cross sections of the 2^1P and 2^3P states have been examined in the light of new and detailed information concerning the cascading to these states from higher states, particularly in the low energy region near onset. Excitation functions of the 1^1S , 1^1D , 3^1S , and 3^1D states have been obtained in this energy range. Absolute measurements of the apparent cross sections of 22 of these states have been presented. These measurements have allowed the calculation of the electron excitation cross sections of the 2^3P and 2^1P states after the latter state had been corrected for imprisonment. The electron excitation cross sections have been compared with theory. The apparent cross section versus pressure curve of the 2^1P state approaches a value expected for nearly complete imprisonment and shows no collisional depopulation effects. The $2^1P \rightarrow 1^1S$ oscillator strength has been obtained from the electron excitation cross section curve. The apparent cross section of the 2^3P state has been used to correct that of the 2^3S near threshold.

The pressure dependence of apparent cross sections has been obtained at 100 eV for the $1P$ states up to $n = 10$, the $1D$ and $3D$ states up to $n = 13$, and the $4F$ state. The low n states show a populating effect which is approximately proportional to the pressure while the high n states show a depopulating effect which is approximately inversely proportional to pressure for the higher pressures. Apparent cross sections for the high nF states, $n = 5$ to 9 , have been obtained at 100 eV and 63μ pressure. The excess population of the $3D$ states at this pressure can be quantitatively accounted for by F state cascade. Indications are that even at low pressure (about 8μ) the F state cascade may account for the excess $3D$ population.

Excitation functions of the $4F$ state have been obtained for pressures of 63 and 8μ . The shape of the function at high pressure suggests that the dominating populating process for this state is excitation transfer from the 4^1P . However, the pressure dependence of the $4F$ apparent cross section makes it necessary to assume an additional populating mechanism. Since theoretical calculations show direct electron excitation to be small, this mechanism is attributed to G state cascade.

Corrections for direct electron excitation and cascade have been made to the apparent cross sections of the 4 , 5 , and $6D$ states at 100 eV and 63μ pressure. It has been found necessary to postulate additional populating mechanisms for these states. Transfer cross sections from the $1P$ to the F and D states have been calculated.

These seem somewhat small for the high nF states and somewhat large for the 3D states (because of the spin rule). On the $n = 4$ level the additional populating mechanism for the 4^3D state is thought to be collisional transfer of excitation from the $4F$ state. This is consistent with the large $4F$ state population, the Wigner spin rule, and the closeness of the energy balance.

By heating the gas in a specially designed electron gun, the temperature dependence of the 4^1P , 3^3D , and 4^3D apparent cross sections has been obtained. Assuming the collisional depopulation of the 4^1P state is to the $4F$, the transfer cross section thus obtained is proportional to the gas temperature. In addition, it has been shown that under the assumption of the collisional ionization of very high n states the 3^3D and 4^3D apparent cross sections are independent of the effects of states of $n > 12$.

It is difficult to assign experimental error to the measurements reported in this paper. In many cases comparison with other experiments and with theory is not possible. Since the apparent cross section is the fundamental experimental quantity whose manipulation leads to the results reported herein, an estimate of its error would be useful.

The data in Table I and in Figure 17 were compared for the $3, 4, 5, 6^3D$ and the $3, 4^1D$ by converting the 100 eV data to peak value apparent cross section using excitation functions obtained at 5μ pressure. The data were taken several weeks apart. The maximum deviation from the mean was 5.5 per cent and the average was 3.7 per cent.

The data of St. John, Miller, and Lin was compared with that of Table I for the 3, 4, and 5¹S, ³S, and ¹D. The ³D was not compared because of its strong pressure dependence even at low pressure. The maximum deviation from the mean was 11.5 per cent and the average was 6.0 per cent. The data of Table I shows in general good straight line fits when $Q'(nK)$ is plotted versus n on log-log paper. Although there may be no a priori reason for this to be so, it does indicate some degree of consistency.

Errors in the theoretical transition probabilities used probably are no more than ± 10 per cent for low n states. For calculations involving the 2³P, 3¹D, 3³D, 3¹S, 3³S, and 4F states, such as cascade analysis, these errors are minimized since the branching ratios involved are unity.

Error limits on measurements involving considerable noise such as low pressure infrared and weak (high n) transitions in the visible may vary from ± 20 per cent to ± 50 per cent.

LIST OF REFERENCES

1. A. H. Gabriel and D.W.O. Heddle, Proc. Roy. Soc. (London) A258, 124 (1960).
2. R. M. St. John, C. C. Lin, R. L. Stanton, H. D. West, J. P. Sweeny, and E. A. Rinehart, Rev. Sci. Instr. 33, 1089 (1962).
3. H. D. West, Master's Thesis, "Automatic Processing of Data on the Excitation of Helium by Electron Impact", University of Oklahoma, Norman, Oklahoma (1962).
4. J. C. DeVos, Physica 20, 690 (1954).
5. R. M. St. John, F. L. Miller, and C. C. Lin, Phys. Rev. 134, A888 (1964).
6. C. Smit, H.G.M. Heideman, and J. A. Smit, Physica 29, 245 (1963).
7. H.S.W. Massey and B. L. Moiseiwitsch, Proc. Roy. Soc. (London) A258, 147 (1960).
8. A. V. Phelps, Phys. Rev. 110, 1362 (1958).
9. H.S.W. Massey and C.B.O. Mohr, Proc. Roy. Soc. (London) A140, 613 (1932).
10. L. A. Vainshtein and G. G. Dolgov, Optics and Spect. 7, 1 (1959).
11. H.R.M. Moussa, Research Report from Institute for Atomic and Molecular Physics, Amsterdam, Netherlands (1967).
12. L. Vriens, Physica 31, 385 (1965).
13. A. M. Skerble and E. N. Lassettre, J. Chem. Phys. 40, 1271 (1964).
14. J. Geiger, Z. Physik 175, 350 (1963); 177, 138 (1964); and 181, 413 (1964).

15. B. Schiff and C. L. Pekeris, Phys. Rev. 134, A640 (1964).
16. N. F. Mott and H.S.W. Massey, "The Theory of Atomic Collisions", 3rd ed. p. 328, Oxford University Press (1965).
17. V. I. Ochkur and V. F. Brattsev, Optics and Spect. 19, 274 (1965).
18. H. K. Holt and R. Krotov, Phys. Rev. 144, 82 (1965).
19. H. Maier-Leibnitz, Z. Physik 95, 499 (1936).
20. G. J. Shulz and R. E. Fox, Phys. Rev. 106, 1179 (1956).
21. R. J. Fleming and G. S. Higginson, Proc. Phys. Soc. (London) 84, 531 (1964).
22. N. F. Mott and H.S.W. Massey, Loc. cit. p. 597.
23. G. J. Shulz and J. W. Philbrick, Phys. Rev. Letters 13, 477 (1964).
24. J. H. Lees and H.W.B. Skinner, Proc. Roy. Soc. (London) A137, 186 (1932).
25. W. Maurer and R. Wolf, Z. Phys. 115, 410 (1940).
26. R. M. St. John and R. G. Fowler, Phys. Rev. 122, 1813 (1961).
27. D. R. Bates, Disc. Far. Soc. 33, 7 (1962).
28. R. M. St. John and T. W. Nee, J. Opt. Soc. Am. 55, 426 (1965).
29. R. B. Kay and R. H. Hughes, Phys. Rev. 154, 61 (1967).
30. P. T. Smith, Phys. Rev. 36, 1293 (1930).
31. F. E. Niles, "Compilation of Helium Transition Probabilities", Report No. 1354, U. S. Army Material Command, B.R.L., Aberdeen Proving Ground, Md., 1967.

32. E. U. Condon and G. H. Shortley, "The Theory of Atomic Spectra", p. 131, Cambridge Univ. Press, London and New York, 1951.
33. W. L. Wiese and M. W. Smith, "Atomic Transition Probabilities", National Bureau of Standards Research Report, 1966.
34. D. R. Bates and A. Damgaard, Phil. Trans. A212, 101 (1949).
35. Chun C. Lin and R. G. Fowler, Ann. Phys. (New York) 15, 461 (1961).
36. M. Goodrich, Phys. Rev. 52, 259 (1937).
37. J. Frenkel and S. Bobkovsky, Physikalische Zeitschr, der Sovjetunion 5, 464 (1934).
38. A. Burgess, Monthly Not. Roy. Astron. Soc. 69, 1 (1964).
39. D. R. Bates "Atomic and Molecular Processes", p. 253, Academic Press, New York and London, 1962.
40. V. E. Cosslett, "Electron Optics", p. 69, Oxford Univ. Press, London and New York, 1946.
41. Englehard Industries, Inc., Inst. and Systems Div., 850 Passiac Ave., East Newark, N. J.
42. R. M. St. John and J. D. Jobe, "Temperature Dependence of Helium Transfer Cross Sections", Univ. of Oklahoma Research Institute Scientific Report. Grant No. AFOSR-252-65, (AD637193), April 1966.
43. L. D. Landau and E. M. Lifshitz, "Statistical Physics", p. 62, Oxford at the Clarendon Press, 1938.
44. M. Kaminsky, "Atomic and Ionic Impact Phenomena on Metal Surfaces", p. 70, Springer-Verlag, Berlin and New York, 1965.